AGU PUBLICATIONS

Tectonics

RESEARCH ARTICLE
10.1002/2014TC003671

Key Points:
- Tectonic quiet period from at least 100 Ma until ~6 Ma of the Litang Plateau
- Late Miocene onset of rapid exhumation due to Litang fault activity
- Litang fault ensures kinematic compatibility between XSH and Red River faults

Correspondence to:
G.-C. Wang and Y.-Z. Zhang,
wgcan@cug.edu.cn;
zyz011051@gmail.com

Citation:
Zhang, Y.-Z., et al. (2015), Timing and rate of exhumation along the Litang fault system, implication for fault reorganization in Southeast Tibet, *Tectonics*, *34*, doi:10.1002/2014TC003671.

Received 3 JUL 2014
Accepted 20 MAY 2015
Accepted article online 25 MAY 2015

Timing and rate of exhumation along the Litang fault system, implication for fault reorganization in Southeast Tibet

Yuan-Ze Zhang[1,2], Anne Replumaz[3,4], Guo-Can Wang[1,2], Philippe Hervé Leloup[5], Cécile Gautheron[6], Matthias Bernet[3], Peter van der Beek[3], Jean Louis Paquette[7], An Wang[1,2], Ke-Xin Zhang[8], Marie-Luce Chevalier[9], and Hai-Bing Li[9]

[1]Center for Global Tectonics, School of Earth Sciences, China University of Geosciences, Wuhan, China, [2]State Key Laboratory of Geological Processes and Mineral Resources, China University of Geosciences, Wuhan, China, [3]ISTerre, Université Grenoble Alpes, Grenoble, France, [4]CNRS, ISTerre, Grenoble, France, [5]Laboratoire de géologie de Lyon, CNRS UMR 5570, Université de Lyon, Université Lyon1–ENS Lyon, Villeurbanne, France, [6]UMR GEOPS Geoscience Paris-Sud–CNRS-UPS 8148, Université Paris Sud, Orsay, France, [7]CNRS UMR 6524, Université Blaise Pascal, Clermont Ferrand CX, France, [8]State Key Laboratory of Biogeology and Environmental Geology, China University of Geosciences, Wuhan, China, [9]Institute of Geology, Chinese Academy of Geological Sciences, Beijing, China

Abstract The Litang fault system that crosses the Litang Plateau, a low relief surface at high elevation (~4200–4800 m above sea level) that is not affected by regional incision, provides the opportunity to study exhumation related to tectonics in the SE Tibetan Plateau independently of regional erosion. Combining apatite and zircon fission track with apatite (U-Th)/He thermochronologic data, we constrain the cooling history of the Litang fault system footwall along two transects. Apatite fission track ages range from 4 to 16 Ma, AHe ages from 2 to 6 Ma, and one zircon fission track age is ~99 Ma. These data imply a tectonic quiet period sustained since at least 100 Ma with a slow denudation rate of ~0.03 km/Ma, interrupted at 7 to 5 Ma by exhumation at a rate between 0.59 and 0.99 km/Ma. We relate that faster exhumation to the onset of motion along the left-lateral/normal Litang fault system. That onset is linked to a Lower Miocene important kinematic reorganization between the Xianshuihe and the Red River faults, with the eastward propagation of the Xianshuihe fault along the Xiaojiang fault system and the formation of the Zhongdian fault. Such strike-slip faults allow the sliding to the east of a wide continental block, with the Litang fault system accommodating differential motion between rigid blocks. The regional evolution appears to be guided by the strike-slip faults, with different phases of deformation, which appears more in agreement with an "hidden plate-tectonic" model rather than with a "lower channel flow" model.

1. Introduction

The indentation of Asia by India resulted in crustal deformation of both continents, causing the buildup of the Earth's largest and highest orogenic plateau. While away from the collision front, the eastern margin of the Tibetan Plateau shows a steep topographic slope at the level of a main thrust zone between the Longmen Shan and the Sichuan basin (Figure 1a). Farther south, the topographic transition from high to low topography is more gradual between the Litang Plateau and the Yangtze Platform (Figure 1a). The Litang Plateau, southeastern prong of the Tibetan Plateau, shows a low relief, high-elevation (~4500 m) surface locally deeply incised by large rivers (i.e., Yalong, Jinsha) (Figure 1a). The regional GPS velocity field shows southeastward motion with respect to Eurasia at a rate of ~15 mm/yr of the whole Litang Plateau south of the left-lateral Xianshuihe fault (XSHF) [e.g., *Zhang et al.*, 2004; *Liang et al.*, 2013] (Figure 1b). This suggests that the plateau is presently growing toward the southeast in that zone. However, the history of that growth greatly varies between authors implying radically different driving mechanisms, making this region critical location for discussing the models of the Tibetan Plateau formation.

In some models the main driving forces are the boundary stresses related to the motion between India and Asia. The Asian deformation follows an "hidden plate-tectonic" pattern with lithospheric blocks bounded by faults where most deformation is localized [e.g., *Tapponnier et al.*, 2001]. Hundreds of kilometers long strike-slip faults would allow the motion of wide continental blocks, such as the Indochina block southeastward extrusion along the left-lateral Ailao-Shan Red River fault during the Oligo-Miocene

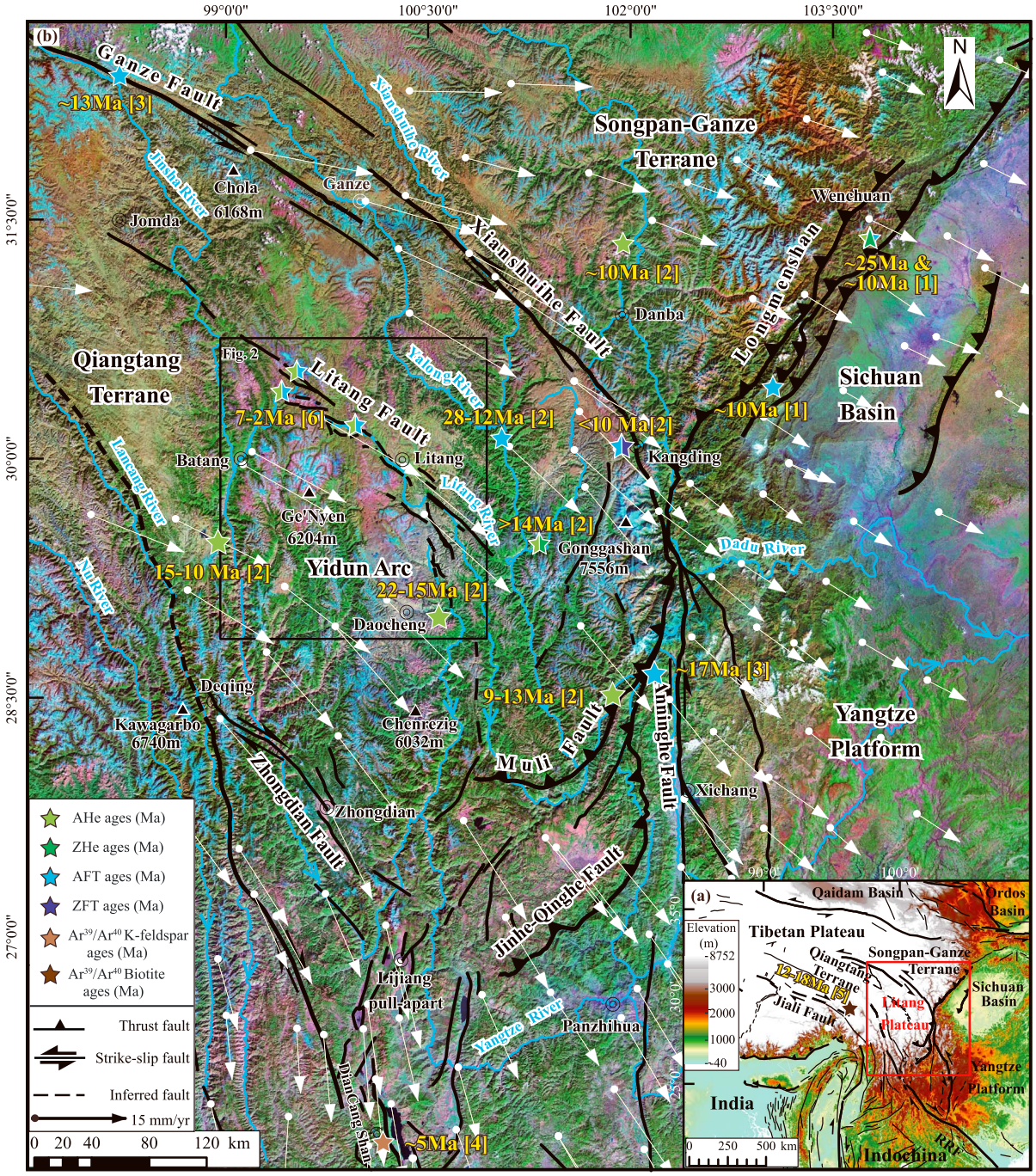

Figure 1. Tectonic setting of Southeast Tibet. (a) Central and eastern Tibetan Plateau topography and tectonic framework. (b) Active faults drawn from Landsat image mosaic (in the background), modified after *Leloup et al.* [1995] and *E. Wang et al.* [2012]; rectangle indicates the Figure 1b. The white arrows are GPS vectors with respect to fixed Eurasia from *Copley* [2008]. The black frame corresponds to Figure 2b. The blue solid lines are rivers. The stars synthesize thermochronological rapid cooling ages from (1) *Arne et al.* [1997], *Kirby et al.* [2002], *Godard et al.* [2009], and *E. Wang et al.* [2012]; (2) *Xu and Kamp* [2000], *Clark et al.* [2005], *Ouimet et al.* [2010], *Wilson and Fowler* [2011], and *Tian et al.* [2014]; (3) *Wang et al.* [2009], *S. Wang et al.* [2012]; (4) *Leloup et al.* [1993, 2001]; (5) *Lee et al.* [2003] and *Lin et al.* [2009]; and (6) this study.

[e.g., *Tapponnier et al.*, 1986; *Leloup et al.*, 1995, 2001] and the Tibet eastward extrusion along the Altyn Tagh fault during the Plio-Quaternary [e.g., *Mériaux et al.*, 2012]. The strike-slip faults also allow transferring some of the thickening far from the Indian indenter, north and east [e.g., *Meyer et al.*, 1998; *Tapponnier et al.*, 2001]. Southeast of the Litang Plateau upper crustal thickening would have occurred during the Miocene along the Muli and Jinhe-Qinghe thrust systems at the end of the XSHF [e.g., *Liu-Zeng et al.*, 2008] (Figure 1b).

Such topography has been dissected during the Miocene, by the rivers flowing out the plateau [*Liu-Zeng et al.*, 2008; *Tian et al.*, 2014].

In other models, the main driving forces are the buoyancy forces resulting from the high elevation and large crustal thickness of the Tibetan Plateau [e.g., *Beaumont et al.*, 2004; *Royden et al.*, 1997, 2008]. In such models, uplift of the eastern Tibetan Plateau would result from outward lower crustal viscous flow from the plateau center. This would lead to regional crustal thickening unrelated to shortening and thrust faulting [e.g., *Clark and Royden*, 2000]. In the Litang area such flow would have induced the uplift of a flat morphologic surface initially close to sea level, a "relict peneplain," in the late Miocene (9–13 Ma), contemporaneous of the deep incision of the river network [e.g., *Royden et al.*, 1997; *Clark et al.*, 2006]. Normal faulting earthquakes with fault planes perpendicular to the flow, occurring near the edge of the flat top of the plateau, could be caused by extension in the downslope direction where the topographic gradient is maximum [*Copley*, 2008]. Farther southeast, normal faulting earthquakes with fault planes parallel to the flow could be caused by the divergence of the flow where it spreads out at low elevation [*Copley*, 2008]. Other models infer that the two different mechanisms may have succeeded through time, and channel flow may have followed eastward extrusion of Indochina [*Schoenbohm et al.*, 2006].

In this paper, we focus on the Litang fault system that crosses the Litang Plateau. That part of the plateau is not crossed by deeply incised valleys, providing the opportunity to study the tectonic exhumation outside of the influence of the main rivers. First, we precisely map the trace of this complex fault system (Figure 2), previously often presented as a simple continuous fault trace [e.g., *Wilson and Fowler*, 2011; *Clark et al.*, 2005; *Tian et al.*, 2014]. We use morphology and striations on fault planes to show that the Litang fault is a normal fault system with a left-lateral component, in contradiction with some previous studies [*Xu et al.*, 2005]. Second, using thermochronologic data and thermokinematics modeling, we constrain the timing of fault activity, the rate of footwall exhumation, and the onset of the local incision. Finally, we discuss the Neogene kinematics of the fault zone in the frame of active deformation and incision in SE Tibet and compare it with prediction of the various models.

2. Geological Setting

2.1. The Litang Plateau

The Litang Plateau is characterized by a high-altitude surface between 4200 and 4800 m with a relief of less than 300 m, away from the deeply incised Jinsha and Yalong rivers (Figure 2a). The boundary between the Songpan-Ganze and Qiangtang terranes straddles the Litang Plateau (Figure 1). In that area the boundary strikes approximately N-S and corresponds to the Triassic Yidun arc, bounded to the west by the east dipping Jinsha suture zone and to the east by the west dipping Ganze-Litang suture [e.g., *Reid et al.*, 2005b]. The western part of the Yidun Arc is composed of Paleozoic rocks, while the eastern one is composed of Triassic clastic and volcanic deposits, intruded by the ~300 km long Late Triassic Ganze-Daocheng pluton and Cretaceous granites [e.g., *Chengdu Institute of Geology and Mineral Resources (CIGMR)*, 2004] (Figure 2). The closure of the Jinsha and Ganze-Litang sutures occurred by the Late Triassic [e.g., *Roger et al.*, 2008; *de Sigoyer et al.*, 2014], and since then the area was only affected by brittle deformation [*Reid et al.*, 2005a, 2005b] mostly along strike-slip faults including the left-lateral Litang fault [*Wilson et al.*, 2006].

In order to discuss the kinematics of the Litang fault system in the frame of SE Tibet Cenozoic deformations, we describe below the regional tectonics and the thermochronologic data that help to constrain the main incision and exhumation phases.

2.2. Bounding Faults of the Litang Plateau

The Litang Plateau is bounded to the north by the left-lateral Ganze-Xianshuihe fault (XSHF). Along the Ganze branch, *Wang et al.* [2009] used apatite fission track (AFT) ages to suggest that the fault was active at ~12.8 Ma (Figure 1). From whole rock Rb/Sr and U/Pb zircon ages, *Roger et al.*, 1995 dated the Gongga Shan granite located along the sharpest curve of the XSHF at ~12 Ma. Interpreting this granite as syntectonic led them to propose that strike-slip deformation started at or prior to ~12 Ma. Using punctual U/Pb zircon data *Li and Zhang* [2013] propose a more complex history where the Gongga Shan granites result from an early Oligocene (32–27 Ma) migmatization and a Miocene (18–12 Ma) magmatic phase, cut by the left-lateral XSHF since 12–10 Ma. Southeastward, the XSHF splits in several strike-slip branches along the Xiaojiang

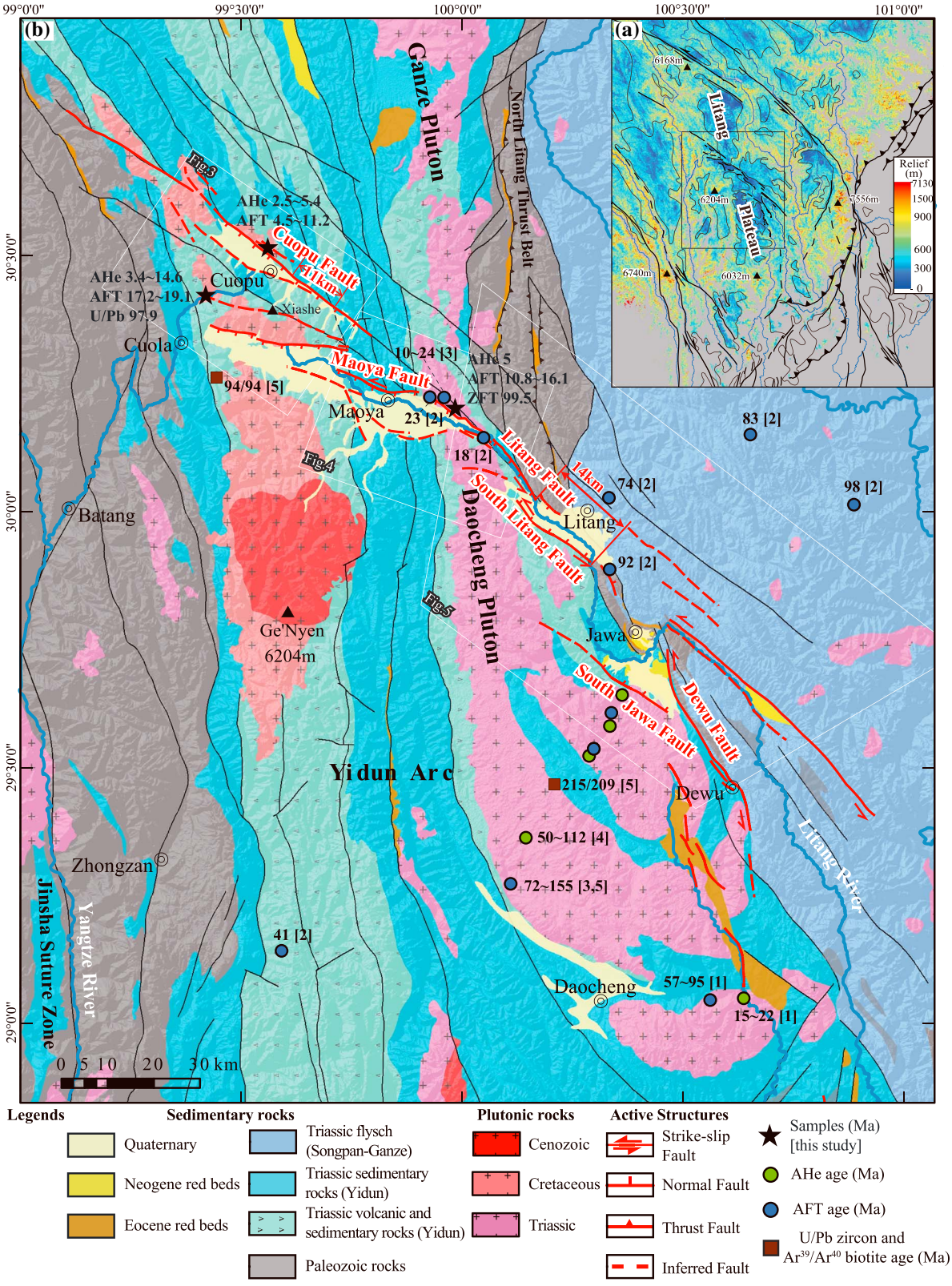

Figure 2. Tectonic and geologic map of Litang Fault Zone and its vicinity in the eastern Tibetan Plateau. (a) Relief map (derived from ~30 m digital elevation model (DEM) calculated over a domain with radius of 1 km with the altitude >3500 m asl. Relict surface (black outlines) is identified by *Clark et al.* [2006]. (b) Geology is modified from *CIGMR* [2004], *BGMR* [1991], and *A. Wang et al.* [2012]. Existing geochronological and thermochronological ages from *Tian et al.* [2014] (1), *Wilson and Fowler* [2011] (2), *Lai et al.* [2007] (3), *Clark et al.* [2005] (4), and *Reid et al.* [2005a, 2005b] (5). The black stars indicate results from this study. SRTM relief in background.

transtensive fault system [e.g., *Allen et al.*, 1991] and connects to the Muli and Jinhe–Qinghe fault thrust systems [*Liu-Zeng et al.*, 2008] (Figure 1). From an altitude versus AFT age relationship, *S. Wang et al.* [2012] infer that the Jinhe-Qinghe thrust was activated at 17 ± 2 Ma. They further suggest that the Jinhe-Qinhhe thrust was abandoned at ~5 Ma when the XSHF propagated toward the south along the Xiaojiang fault system.

To the southwest, the plateau is bounded by the right-lateral Zhongdian fault, connecting to the right-lateral Red River fault (RRF) by the pull-apart of Lijiang, a complex extensive zone (Figure 1) [*Leloup et al.*, 1995]. The onset age of the Zhongdian fault is unknown, but the cooling history of the Diancang Shan range bounding to the south the Lijiang pull-apart (Figure 1) suggests that this extension activated at ~5 Ma [*Leloup et al.*, 1993]. The reactivation of the dextral RRF has been inferred from the age of onset of folding in the Tonkin gulf ~1000 km farther southeast absorbing the dextral motion of the fault, first estimated at ~5 Ma [*Replumaz et al.*, 2001; *Schoenbohm et al.*, 2006], recently reestimated at 8–9 Ma using a more detailed seismic data set [*Fyhn and Phach*, 2015]. The AFT ages from the Ailao Shan range along the RRF suggest that the fault could be active since 10–11 Ma [*Leloup et al.*, 2001].

2.3. Erosion and Incision of Southeast Tibet

Previous low-temperature thermochronological studies showed that wide portions of the low relief and high-elevation Litang Plateau have experienced little denudation since the Cretaceous (see ages on Figure 2). For the Ganze pluton, AFT ages range from 124 to 154 Ma [*Lai et al.*, 2007], while they range from 72 to 155 Ma in the Daocheng pluton [*Reid et al.*, 2005a; *Lai et al.*, 2007], suggesting less than 3 km of exhumation since the Cretaceous. Such slow exhumation is confirmed by apatite (U-Th)/He (AHe) ages of the Daocheng pluton that range from 50 to 112 Ma, corresponding to exhumation at rates ≤0.02 mm/yr until present [*Clark et al.*, 2005]. Accordingly, AFT ages from Triassic sandstone to the east of the Litang fault are older than 70 Ma [*Wilson and Fowler*, 2011]. However, Miocene AFT and AHe ages are reported from areas close to the main fault zones and the main rivers [e.g., *Lai et al.*, 2007; *Wilson and Fowler*, 2011] (Figure 1).

Five large rivers flow out of the SE Tibetan Plateau: the Jinsha River (local name of the Yangtze) and two of its tributaries, the Dadu, and Yalong rivers, the Lancang River (local name of the Mekong), and the Nu River (local name of the Salween). They have cut deep gorges, locally more than 2000 m below the mean elevation (Figure 1). Assuming a short lag time between uplift and incision, the age of the river incision could serve as a proxy to that of the surface uplift. Low-temperature thermochronological ages record rapid incision along the Dadu, the Jinsha, and the Yalong Rivers in the late Miocene, between 9 and 13 Ma, with rates on the order of 0.2–0.5 mm/yr [*Schoenbohm et al.*, 2004; *Clark et al.*, 2005; *Ouimet et al.*, 2010] (Figure 1). Older early Miocene ages, spanning between 15 and 22 Ma, have been documented near Daocheng along a tributary of the Yangtze river incising the pluton (Figure 2), which has been interpreted as a spatial variation of the local regressive incision history of the Eastern Tibetan Plateau [*Tian et al.*, 2014].

3. The Litang Fault system

The Litang fault system crosses the Litang Plateau outside of the zone affected by deep incision, providing the opportunity to study exhumation linked to faulting independently of the regional erosion. Our mapping, based on morphologic criteria from satellite imagery and field studies, shows that the Litang fault system consists of several NW-SE fault segments running for ~190 km parallel to the XSHF, then progressively turning N-S (Figure 1). A normal component of motion along some fault segments exhumes rocks in the footwall and opens wide sedimentary basins along the hanging wall (Figure 2). The maximum elevation of the mountain ranges decreases from NW to SE, from ~5800 m near Cuopu, where the range rises ~1700 m above the mean elevation of the plateau, to ~5000 m near Maoya and Litang, where the ranges rise ~1000 m above the plateau. From NW to SE, the Cuopu, Maoya, and Litang basins are mapped as Quaternary (Figure 2). The depth of the basins is unknown, as well as the age of the bottom sediments. To the SE, the Jawa basin exposes Neogene fluvial-lacustrine sediments, between 300 and 400 m thick, dated at 4.3 ± 0.4 Ma [*Zhou et al.*, 2005], which unconformably overlain Paleogene red beds and Paleozoic sequences (Figure 2). Morphologic evidences for left-lateral motion along most segments of the Litang fault system have also been documented from seismic surface rupture as well as offset morphologic marker, such as alluvial fan [*Xu et al.*, 2005].

Northwest of the Litang fault zone, the North Cuopu fault separates the >5800 m high peaks of Cretaceous porphyritic biotite monzonite granite of the Garrapunsum range from the Cuopu basin (Figure 3). Large,

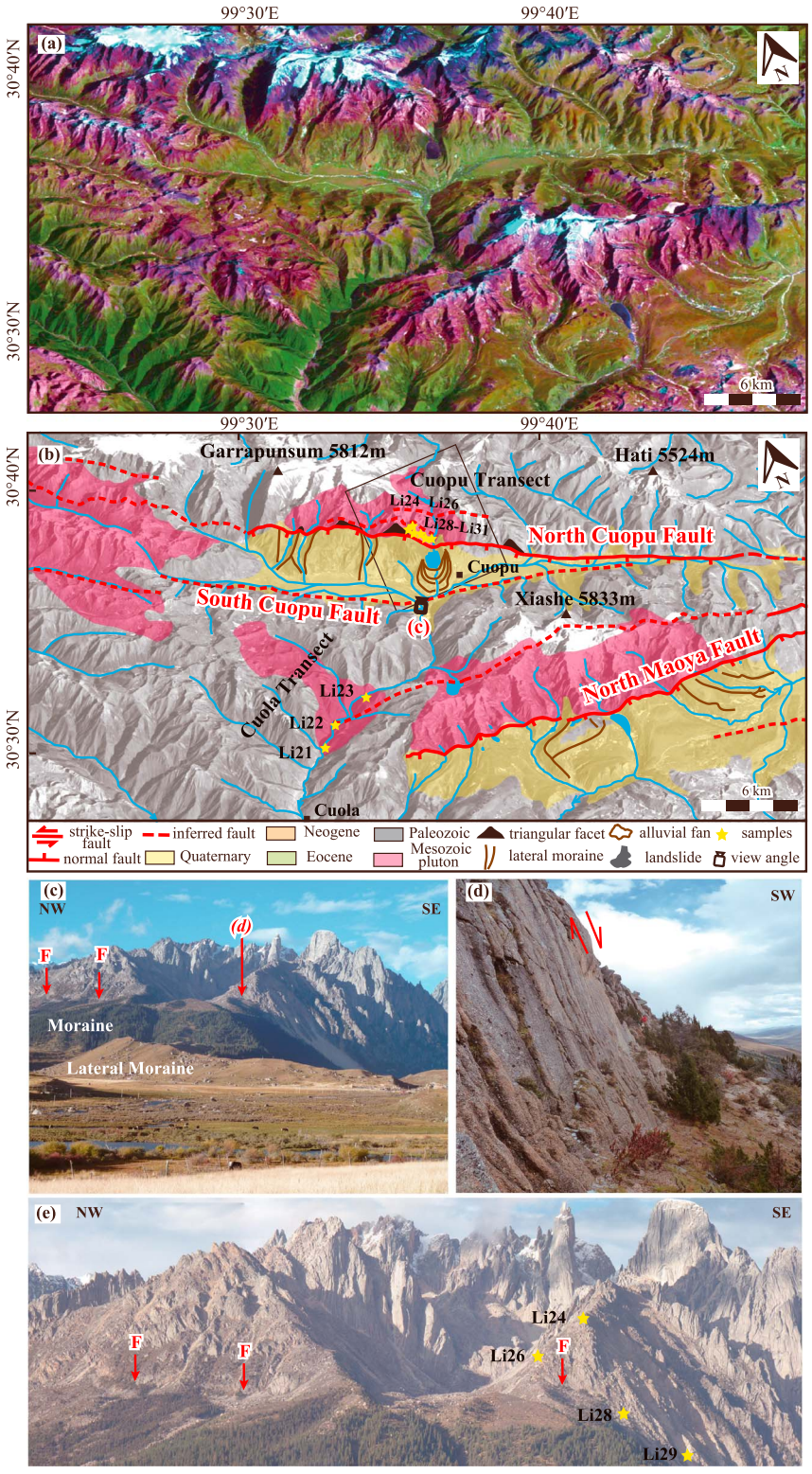

Figure 3. Morphology and geology of the Cuopu and Cuola transects. (a) Oblique 3-D view of a Landsat Enhanced Thematic Mapper (ETM) image draped on topography (Advanced Spaceborne Thermal Emission and Reflection Radiometer (ASTER) DEM). (b) Same view as Figure 3a but with simplified geology and sample locations (yellow stars). The black box corresponds to Pecube model zone. (c) North Cuopu fault between Cretaceous monzonitic granite (high peaks) and Quaternary moraines. The fault is shown by red arrows. (d) North Cuopu fault plane, view from NW. (e) Locations of the four highest samples of the Cuopu transect.

well-preserved latero-frontal glacial moraine deposits cross the entire Cuopu basin in a NS direction. A steep fault plane marks the limit between the granite and the moraine deposits, indicating vertical normal motion (Figures 3c–3e). At this location the granite is cataclased along planes trending N135° and dipping 80° to the SW (Figure 3d). The moraines do not seem to cross the fault, appearing only in the hanging wall, and thus no vertical offset of the moraines can be quantified. The minimum vertical offset can be estimated at 1700 m, corresponding to the altitude difference between the Garrapunsum summit (~5800 m) and the basin (~4100 m). The depth of the Cuopu basin should be added to this minimum vertical offset but is unknown. No evidence for morphological horizontal offset has been found, as the river that incised the granite is not offsetted (Figure 3a), but SE of the range the local geological map suggests a ~11 km left-lateral offset of Triassic beds [*Bureau of Geology and Mineral Resources (BGMR)*, 1991], which may be interpreted as a maximum left-lateral offset (Figure 2). South of the basin, smooth triangular facets suggest the presence of a smaller conjugate normal fault, the South Cuopu fault (Figure 3b).

Southeast of the Cuopu basin, the North Maoya fault separates the 55 km long Maoya basin from the 5833 m high peaks of the Cretaceous Xiashe granite (Figure 3b) to the west and the ~5000 m high Jiaolongworuma granite to the east (Figure 4b). The morphology is one of an active normal fault with spectacular triangular facets (380–620 m high) and a curvilinear map trace. A ~10–20 m high fault scarp offsetting several alluvial fans is visible along most of the northern edge of the Maoya basin at the foot of the triangular facets and attests to recent normal faulting activity (Figure 4c). At our sampling site (Figure 4c), *Xu et al.* [2005] measured a 17 ± 3 m vertical offset, interpreted as due to a reverse fault, of an alluvial fan dated at 9.4 ± 0.42 ka B.P. by thermo-luminescence, implying a vertical rate of 1.8 ± 0.6 mm/yr. They used beheaded superficial gullies at the top of the fan to suggest a 38 ± 7 m left-lateral offset on the fault. At the same site we measured a smaller vertical offset (~12 ± 2 m) by cinematic GPS, dated at ~20 ka by ^{10}Be cosmogenic method (Marie-Luce Chevalier, personal communication), implying a ~0.6 mm/yr vertical rate. We find no systematic offset of superficial gullies, rivers incising the Xiashe granite, or fan edges (Figure 4a), and we conclude to the absence of morphological evidence for recent left-lateral faulting along the North Maoya fault. However, the western and eastern boundaries of the Upper Triassic Garze-Daocheng pluton show an ~6.5 km and ~6.1 km left-lateral offset, respectively (Figure 4b). At a broader scale, Paleozoic rocks overlain by Eocene red bed basins lay along the eastern margin of the pluton showing a 14 km left-lateral offset across the Litang fault zone (Figure 2). As for the Cuopu basin, minor active normal faults bound the basin to the south (Figure 4b).

Northwest of the Litang basin, a segment of the Litang fault has a linear NW-SE morphologic trace with well-preserved seismic surface ruptures that have been attributed to a ~*M*7 earthquake occurring in 1890 [*Xu et al.*, 2005]. The rupture zone shows left-lateral, possibly coseismic, gully offsets of ~1 m (Figure 5d) and ~3 m, possibly cumulative, relative vertical uplift of the NE footwall (Figure 5c). Possible larger cumulative left-lateral offsets up to 40 ± 4 m of ~10 ka alluvial terraces have been inferred corresponding to a left-lateral rate of 4.1 ± 1 mm/yr [*Xu et al.*, 2005]. The trace of the strike-slip fault is difficult to follow across the Litang basin. The SW part of that fault shows a normal scarp west of Benge village, and a parallel strike-slip fault, with no clear morphologic offset. A trench across the strike-slip fault reveals several earthquakes since 30,000 years, with coseismic slips of 2 to 4 m, and a vertical fault plane dip, interpreted as reverse by the authors of the paper [*Xu et al.*, 2005]. The basin is bounded to the south by the South Litang fault, with clear but smooth triangular facets culminating at 5064 m in a small granitic pluton (Figure 5b).

Further SE, the Jawa basin is a triangular Eocene-Quaternary basin bounded to the NE by the NNW-SSE Dewu fault (Figure 2) with a prominent morphologic trace (Figures 5a and 5b). The 25 May 1948 earthquake (*M*7.3) ruptured the Dewu fault over ~40 km, with a maximum coseismic left-lateral offset of 4.3 m and a vertical one of 1 m [*Xu et al.*, 2005]. A thermoluminesence age of 12.12 ± 0.63 ka B.P. for an alluvial fan offset by 51 ± 10 m suggests a left-lateral cumulative slip-rate of 4.3 ± 1.0 mm/yr [*Xu et al.*, 2005]. The southern edge of the basin is a steep NW-SE trending slope, along which a N105° striking and 35°N dipping fault plane crops out (Figure 5e). That fault plane shows two sets of slickenside striations, a left-lateral one with a pitch of 20°W and a normal one with a pitch of 90°, the latter clearly cutting the left-lateral striation (Figure 5f). These crosscutting relationships show that left-lateral motion occurred prior to the normal motion, possibly with a progressive rotation from one orientation to the other.

These morphologic and structural observations imply that the Litang fault system is a transtensive left-lateral fault system. The North Cuopu, North Maoya, and South Jawa fault morphology shows pure normal motion

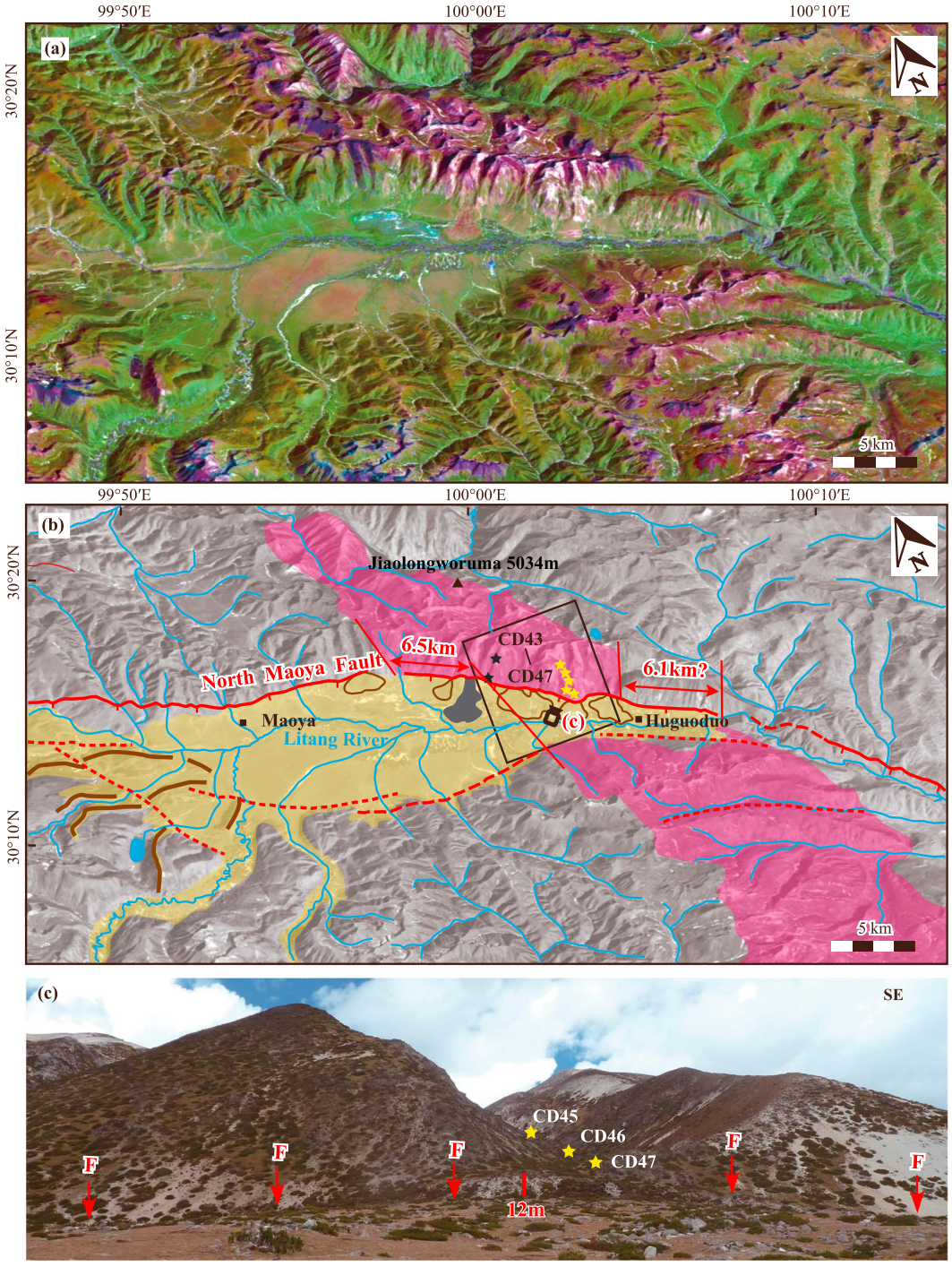

Figure 4. Morphology and geology of the Maoya transect. (a) Oblique 3-D view of a Landsat ETM image draped on topography (ASTER DEM). (b) Same view as Figure 4a but with simplified geology and sample locations (yellow stars from this study; black stars show *Lai et al.* [2007] transect). Same legend as Figure 3b. Note the ~6 km pluton offset across the North Maoya fault. The black box corresponds to Pecube model zone. (c) Spectacular triangular facets (~350 m high) and ~12 m high fault scarp between Triassic granodiorite and Quaternary sediments along the North Maoya fault (red arrows). Three lowest samples of the Maoya transect are shown (yellow stars).

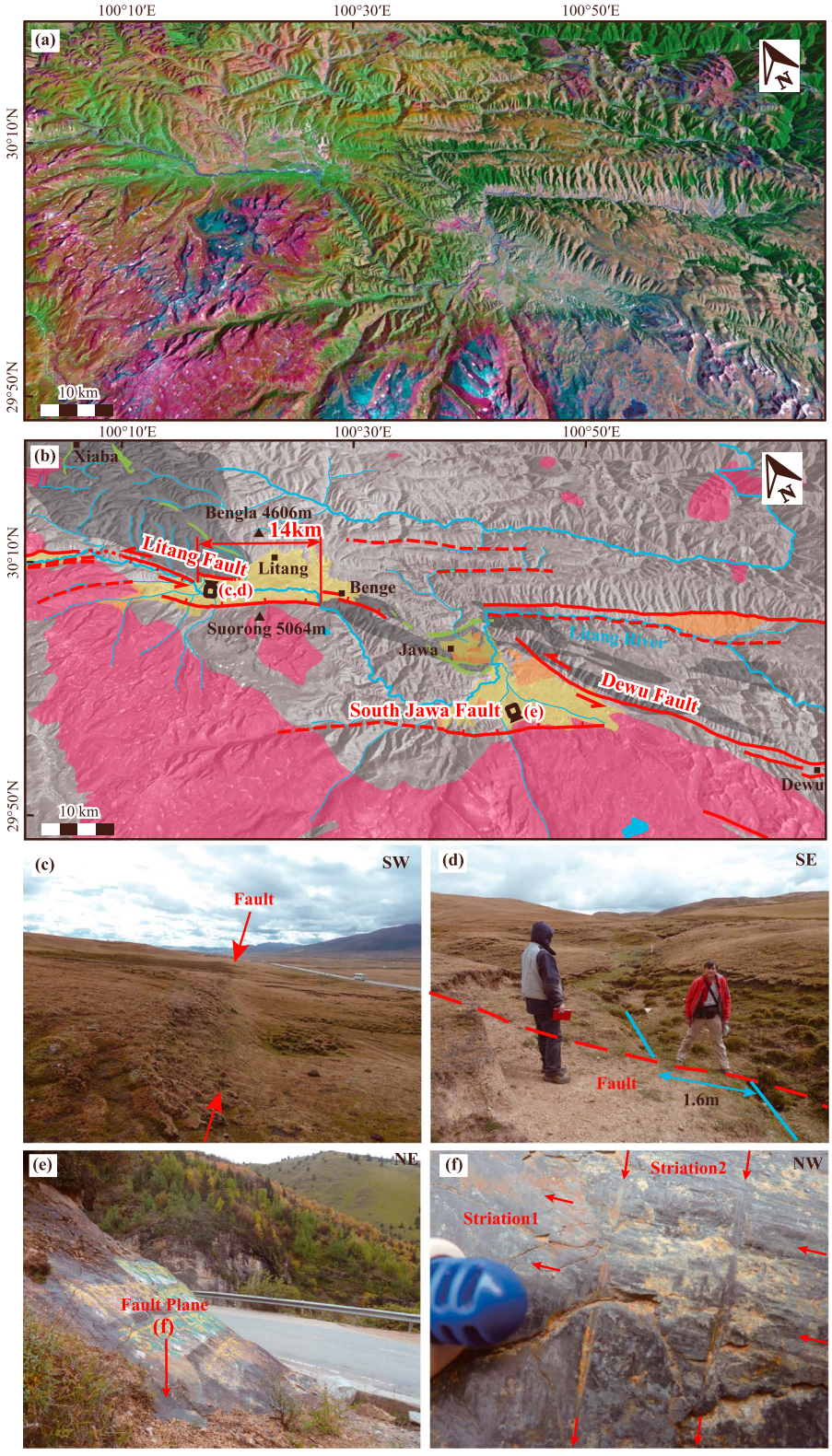

Figure 5. Morphology and geology of the Litang and Jawa basins. (a) Oblique 3-D view of a Landsat ETM image draped on topography (ASTER DEM). (b) Same view as Figure 5a but with simplified geology. Same legend as Figure 3b. (c) Seismic surface rupture along the Litang fault. View toward the SE. (d) Approximately 1.6 m left-laterally offset gully across the Litang fault. View from SW. (e and f) South Jawa fault plane. (e) View from SE (f) close-up showing the two striations: first strike-slip and second down-dip.

since at least ~20 ka but long-term (Cenozoic) left-lateral offset between 6 and 14 km. The Litang and Dewu faults show left-lateral and normal earthquake ruptures, with unclear cumulative offsets.

4. Thermochronology and Geochronology

In this paper, we focus on the granitic ranges exposed along the Litang fault system to constrain the exhumation rate and onset of motion along the fault segments, considering that the background erosional exhumation is negligible away from the deeply incised valleys.

4.1. Sampling Strategy

We collected 14 samples from the granitic ranges exhumed in the footwall of the Litang fault system. We sampled only Mesozoic granitic rock and use AFT and AHe thermochronology to constrain cooling in the upper crust. The AFT and AHe thermochronometer closure temperatures are about 120°C and 75°C, respectively, with partial annealing zone between 60–120°C and 50–90°C, respectively, depending on cooling rate [*Gallagher et al.*, 1998; *Farley*, 2000; *Flowers et al.*, 2009; *Gautheron et al.*, 2009]. Therefore, they constrain exhumation and denudation in the shallow crust from depths between ~1.5 and ~3.5 km, depending on the local geothermal gradient. We sampled two transects in the footwall of the Maoya and Cuopu faults (Figure 2), dense enough to infer the exhumation history using kinematics models. We sampled one transect along the Cuola River crossing the Xiashe range (Figure 3) to constrain the Cuola River incision initiation and discuss the timing of the eastern Tibetan Plateau river incision.

We obtained only one zircon fission track (ZFT) age that helped to constrain the cooling history of the deeper crust. We also report one U/Pb age on the Xiashe granite mapped as Cretaceous [*BGMR*, 1991] to ensure its crystallization age.

4.2. Apatite and Zircon Fission Track Analysis

Samples were prepared and analyzed at the Institut des Sciences de la Terre (ISTerre) thermochronology laboratory (Grenoble, France), using the external detector method described by *Fillon et al.* [2013]. Fission tracks were counted in at least 20 grains for each sample. Fission track ages were calculated using the Zeta-calibration method and the standard fission track age equation [*Hurford and Green*, 1982]. The χ^2-test and age dispersion were used to assess the homogeneity of AFT ages [*Galbraith and Green*, 1990; *Galbraith and Laslett*, 1993]. The weighted mean apatite and zircon Zeta value for Y. Zhang are respectively 311 ± 8.5 (IRMM540R dosimeter glass) and 145 ± 2.8 (CN1 dosimeter glass).

All horizontal confined track lengths parallel to the crystallographic *c* axis and the lengths of the track etch pits (Dpar) were measured on datable grains. However, owing to the small size (mostly less than 80 μm) and the low uranium content of apatite grains, we did not obtain sufficient track lengths to be statically representative. Large Dpar values are generally positively correlated with high chlorine contents in apatite [*Donelick et al.*, 2005], which is relevant for track annealing as Cl-rich apatites are more resistant to annealing than F-rich apatites and thus have higher closure temperatures. Dpar is thus a valuable estimator of annealing rate of an individual apatite grain [*Carlson et al.*, 1999; *Barbarand et al.*, 2003].

4.3. Apatite (U–Th)/He Analysis

Apatite grains were carefully selected with respect to their morphology at the ISTerre thermochronology laboratory. Each grain was placed into a platinum basket for He analysis at Paris Sud University (Orsay, France), using the method described by *Fillon et al.* [2013]. Two to six replicates were analyzed per sample. The analysis was calibrated using internal and external age standards, including the Limberg Tuff and Durango Tuff. Single-grain AHe ages were corrected by each grain's ejection factor F_T, determined using the Monte Carlo simulation technique of *Ketcham et al.* [2011]; the equivalent-sphere radius has been calculated using the procedure of *Gautheron and Tassan-Got* [2010]. The 1σ error on AHe age is considered to be 9%, reflecting the sum of errors in the ejection-factor correction and age dispersion of the standards.

4.4. Zircon U/Pb Analysis

Sample LI21b was analyzed by laser ablation-inductively coupled plasma-mass spectrometry (LA-ICP-MS) of the Laboratoire Magma et Volcans, Clermont-Ferrand (France). Both Tera-Wasserburg lower intercepts and weighted average $^{206}Pb/^{238}U$ ages were calculated. The details of the analytical methods and settings

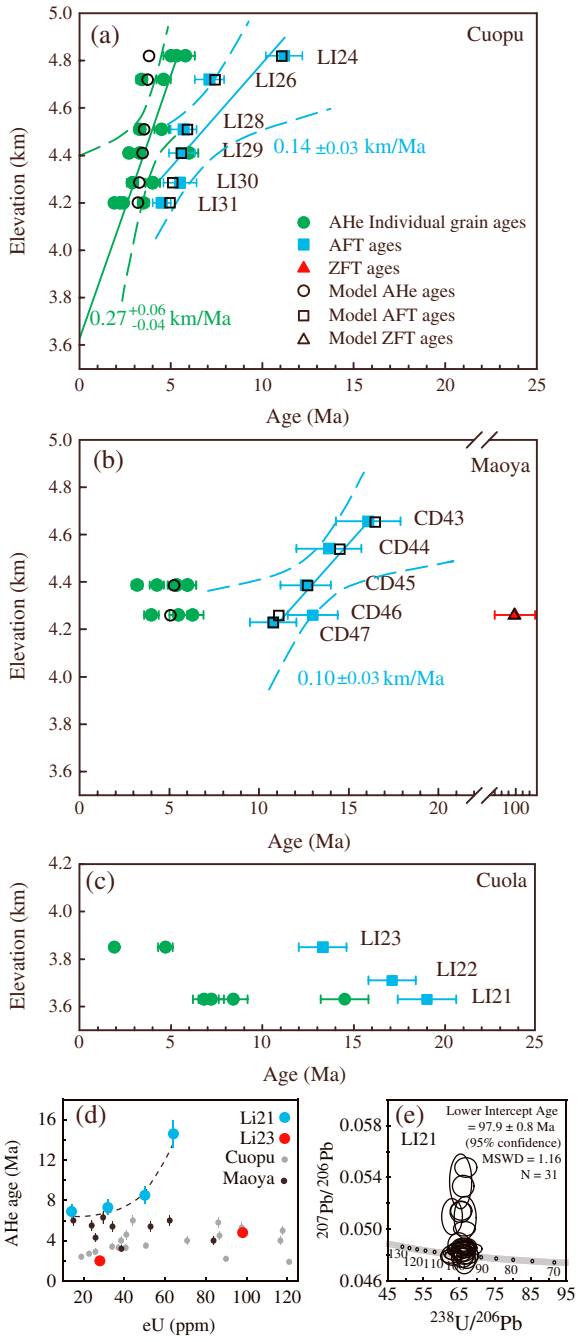

Figure 6. Geochronological data. AHe and AFT ages versus sample elevation relationships with common legend shown in Figure 6a. Data appear in colors while results from Pecube preferred models are empty black symbols. Ages are plotted with 1σ analytical uncertainty. The straight lines are least squares regressions assuming a single exhumation event with 95% confidence interval. (a) Cuopu transect. (b) Maoya transect. (c) Cuola transect. (d) AHe ages plotted as a function of eU content for Cuola transect. The dashed line represents exponential fit to sample LI21. (e) Sample LI21 zircons LA-ICP-MS U–Pb concordia diagram.

have been described by *Paquette and Tiepolo* [2007] and *Valli et al.* [2008]. The U/Pb data summary is given in Table 5, and data are plotted in Figure 6e.

4.5. Data Analysis Methods

For samples collected at various elevations along a short transect, the general increase of thermochronological ages with elevation in a so-called age-elevation relationship (AER) is routinely used to derive rates of exhumation [e.g., *Wagner*, 1981], whereas breaks-in-slope provide information about timing of changes in exhumation rates [e.g., *Fitzgerald et al.*, 1995]. A major unknown in the interpretation of AER is the dimensionality of the model, such as the number of exhumation steps to be fitted [e.g., *Akaike*, 1974; *Schwarz*, 1978]. The Bayesian information criterion (BIC) provides a way to assess the appropriate model complexity [*Schwarz*, 1978]. By calculating the BIC, we test if the age-elevation profiles could be better fitted by two or three independent slope segments than by a single AER, the preferred model being the one yielding the lowest BIC value (for a complete description of the method see *Glotzbach et al.* [2011]).

The AER is influenced by time-varying exhumation and topography effects [e.g., *Mancktelow and Grasemann*, 1997; *Stüwe et al.*, 1994], as well as grain chemistry or size. Quantifying exhumation rates requires that samples have not resided too long in an exhumed partial annealing/retention zone [*Brown et al.*, 1994; *Gleadow and Brown*, 2000] and that closure-temperature isotherms are horizontal or that the sampled profile is perfectly vertical [*Stüwe et al.*, 1994], which is rarely the case in nature. Therefore, we apply the three-dimensional numerical thermal-kinematic code Pecube, described in *Braun et al.* [2012], to account for temporal variations in exhumation rates and paleo-relief, in order to quantify the exhumation history [e.g., *Braun*, 2003; *Braun and Robert*, 2005; *Valla et al.*, 2010]. Pecube is a finite element code that solves the 3-D heat-transport equation and predicts the thermal structure of a crustal block under prescribed spatially and temporally varying kinematic and topographic histories. Pecube uses an inversion algorithm to efficiently sample the multidimensional parameter space and find the parameter values that show the smallest misfit between observed and predicted data (sampling stage [*Sambridge*, 1999a; *Braun et al.*, 2012]). Pecube then extracts statistically robust bounds on optimal parameter

Table 1. Apatite Fission Track Data[a]

Transect	Sample	Location (°E/°N)		Elevation (m)	Grains (N)	ρ_d (10^5 cm^{-2}) (Nd)	ρ_s (10^4 cm^{-2}) (Ns)	ρ_i (10^5 cm^{-2}) (Ni)	U (ppm)	$P(\chi^2)$ (%)	Central Age ± 1σ (Ma)	Dpar ± 1σ (μm)	MTL ± 1σ (μm) (Nl)
Maoya	CD43	99.9807	30.1911	4656	26	8.460 (5406)	12.7 (81)	9.5 (606)	17	99.0	16.1 ± 1.8	1.64 ± 0.03	
	CD44	99.9816	30.1874	4541	27	8.432 (5388)	9.65 (56)	8.32 (483)	15	99.6	13.9 ± 1.8	1.62 ± 0.03	
	CD45	99.9825	30.1846	4387	25	8.404 (5370)	16.1 (88)	15.2 (834)	27	98.3	12.6 ± 1.4	1.72 ± 0.03	
	CD46	99.9814	30.1811	4260	20	8.479 (5417)	17.8 (89)	16.6 (829)	29	99.8	13.0 ± 1.4	2.17 ± 0.03	12.55 ± 0.28 (54)
	CD47	99.9813	30.1805	4230	23	8.376 (5352)	19.8 (72)	21.9 (796)	39	88.5	10.8 ± 1.3	1.83 ± 0.03	
Cuola	Li21	99.3969	30.4144	3630	20	8.310 (5309)	32.6 (156)	20.2 (969)	37	99.7	19.1 ± 1.6	1.54 ± 0.03	
	Li22	99.4133	30.4217	3710	25	8.270 (5284)	35.7 (203)	24.4 (1388)	44	92.4	17.2 ± 1.3	1.58 ± 0.03	
	Li23	99.4426	30.4296	3850	26	8.230 (5258)	29.5 (155)	25.9 (1361)	47	91.0	13.4 ± 1.1	1.60 ± 0.03	
	Li24	99.5478	30.5119	4820	30	8.190 (5233)	17.0 (130)	18.0 (1371)	33	87.8	11.2 ± 1.0	1.48 ± 0.03	
	Li26	99.5461	30.5120	4720	25	8.150 (5207)	11.1 (81)	18.3 (1332)	34	92.3	7.1 ± 0.8	1.54 ± 0.03	
Cuopu	Li28	99.5487	30.5085	4510	25	8.110 (5182)	12.1 (64)	25.0 (1319)	46	97.7	5.7 ± 0.7	1.40 ± 0.03	
	Li29	99.5519	30.5083	4410	29	8.070 (5156)	9.57 (65)	19.8 (1342)	37	97.6	5.6 ± 0.7	1.60 ± 0.03	
	Li30	99.5540	30.5075	4285	24	8.030 (5131)	7.53 (36)	15.8 (755)	30	99.1	5.5 ± 0.9	1.35 ± 0.03	
	Li31	99.5549	30.5068	4200	26	7.990 (5105)	13.1 (72)	33.3 (1823)	62	99.7	4.5 ± 0.5	1.26 ± 0.03	

[a]Note that the brackets show number of tracks counted and measured. Standard and induced tracks were measured on mica external detector ($g = 0.5$) and fossil track densities on internal grain surfaces. All ages in the table are pooled ages, with errors reported at the one sigma level. Abbreviations: $\mu_{s/i/d}$, spontaneous/induced/standard glass track densities; $N_{s/i/d}$, numbers of spontaneous/induced/standard glass tracks; *N*, number of grains; MTL, mean confined horizontal track length; Nl, number of lengths.

values from the ensemble generated by the sampling stage (appraisal stage [*Sambridge*, 1999b; *Glotzbach et al.*, 2011; *Braun et al.*, 2012]). The sampling ensemble is resampled to gain marginal probability density functions of parameter values. Modeling results are visualized as scatterplots together with 1-D and 2-D marginal probability density functions. In the scatterplot, the input variables describe the coordinate system and symbols are colored according to their misfit with cold colors corresponding to low misfits (see section 5). In addition, probable exhumation and relief evolution paths are visualized as synoptic 2-D marginal probability density functions derived from the resampled ensemble.

5. Results: Timing and Rate of Cooling Along the Litang Fault System

From the 14 samples collected along the three profiles, Cuopu, Maoya, and Cuola (see Figure 2 for location), we obtained 14 AFT ages (Table 1), 10 AHe ages (Table 2), and one ZFT age (Table 3). The results are reported in Figure 6. All AFT central ages from the three profiles are Miocene to Pliocene (from 19 to 4 Ma). Chi-square probabilities of all samples are ≫5%, and age dispersions are close to 0, indicating that AFT apparent ages constitute single age populations and suggesting that they experienced a single cooling event [*Galbraith and Laslett*, 1993]. The average AHe ages are systematically <6 Ma, except for the Cuola transect, where they range from 2 to 15 Ma.

5.1. Cuopu Transect

The Cuopu transect is an altitudinal profile in the granite uplifted in the footwall of the north Cuopu fault (Figures 2 and 3). Six samples (LI24, LI26, LI28 to LI31) have been collected from elevations ranging between ~4200 and ~4800 m (Figure 3d). They yield AFT ages between 4.5 ± 0.5 and 11.2 ± 1.0 Ma (Table 1). The ages show a positive correlation with elevation (Figure 6a). All measured Dpar values are less than 1.75 μm and have to be considered as fast-annealing apatites with relatively low closure temperatures [*Donelick et al.*, 2005]. Such apatites are usually rich in F, but no direct chemical measurement has been performed to test it. Assuming a single least squares regression yields a slope of 0.14 ± 0.03 km/Ma (mm/yr), the correlation coefficient (r^2) is 0.87 and the BIC value is 12.1 (Figures 6a and 7b). All samples except for one (LI26) lie within the 95% confidence interval. The relatively old age of LI26 could alternatively be interpreted as the base of an exhumed partial annealing zone, therefore marking the onset of rapid cooling. A two-step age-elevation relationship has a slightly lower BIC value of 11.9, with a recent exhumation rate of $0.22^{+0.13}_{-0.06}$ km/Ma and very slow exhumation (0.02 ± 0.02 km/Ma) between 10 and 7 Ma (Figure 7b). Such a scenario is required only by one sample (LI26) and has to be confirmed by thermochronological modeling taking into account both AFT and AHe results. A three-step AER scenario leads to a higher BIC value of 16, showing that this hypothesis is not supported by our data (Figure 7b).

Table 2. Apatite (U-Th)/He Data[a]

Sample	Grain Replicate	Mass (μg)	Radius (μm)	F_T	4He (nmol/g)	U (ppm)	Th (ppm)	eU (ppm)	Raw Age (Ma)	Corrected Age (Ma ± 1σ)
CD45	A	2.08	42	0.72	0.49	24.9	57.2	38.6	2.3	3.2 ± 0.3
	B	1.44	38.9	0.68	1.04	31.3	90.1	52.9	3.6	5.4 ± 0.5
	C	2.11	44.6	0.70	0.69	21.9	51.5	34.2	3.7	5.4 ± 0.5
	E	2.61	46.9	0.71	0.43	17.7	34.2	25.9	3.0	4.3 ± 0.4
	G	2.11	44.6	0.70	0.34	8.5	27.1	15.0	4.2	6.0 ± 0.5
	H	1.27	36.4	0.65	1.32	39.5	94.9	62.3	3.9	6.0 ± 0.5
CD46	A	1.4	39.1	0.73	0.74	23.1	27.0	29.6	4.6	6.3 ± 0.6
	B	1.11	36.4	0.66	0.47	15.4	35.8	24.0	3.6	5.5 ± 0.5
	C	0.78	33.5	0.65	1.18	58.2	106.7	83.8	2.6	4.0 ± 0.4
LI21	A	2.3	48	0.75	0.40	9.8	18.0	14.1	5.1	6.9 ± 0.6
	B	2.55	45.7	0.75	0.95	21.5	43.3	31.9	5.5	7.3 ± 0.7
	C	2.58	46.7	0.76	3.85	46.7	72.5	64.1	11.1	14.6 ± 1.3
	D	1.53	40.7	0.75	1.74	34.7	64.1	50.1	6.4	8.5 ± 0.8
LI23	B	1.88	45.5	0.74	1.88	71.5	110.5	98.1	3.5	4.8 ± 0.4
	C	1.19	37.7	0.75	0.23	20.4	31.3	28.0	1.5	2.0 ± 0.2
LI24	A	1.84	43.6	0.73	2.29	61.4	234.9	117.7	3.6	5.0 ± 0.4
	C	1.79	42.9	0.76	2.11	45.9	167.6	86.1	4.5	5.8 ± 0.5
	D	1.31	38.6	0.73	2.08	55.3	176.4	97.6	3.9	5.3 ± 0.5
LI26	A	2.61	43.6	0.72	0.46	18.6	64.1	34.0	2.4	3.4 ± 0.3
	B	2.12	43	0.73	0.76	27.4	56.8	41.0	3.4	4.6 ± 0.4
LI28	A	1.77	37.4	0.68	0.50	21.5	80.1	40.7	2.2	3.3 ± 0.3
	B	0.91	34.5	0.73	1.56	44.5	175.8	86.7	3.3	4.5 ± 0.4
LI29	A	3.27	51.9	0.79	0.27	13.1	39.8	22.7	2.2	2.7 ± 0.2
	B	0.749	43.9	2.08	0.52	20.3	70.4	37.2	2.5	3.3 ± 0.3
	D	1.43	41.9	0.67	0.99	22.2	91.3	44.2	4.0	6.0 ± 0.5
LI30	A	1.2	39.4	0.71	1.80	60.1	235.5	116.6	2.8	4.0 ± 0.4
	B	2.33	44.5	0.74	0.31	13.5	51.1	25.8	2.2	2.9 ± 0.3
	C	2.14	45.9	0.79	1.21	36.0	145.1	70.8	3.1	4.0 ± 0.4
	D	1.17	37.3	0.74	0.63	19.5	78.9	38.4	3.0	4.0 ± 0.4
LI31	A	1.11	35.9	0.70	0.18	10.9	33.6	18.9	1.7	2.4 ± 0.2
	B	0.87	34	0.71	0.76	41.5	201.8	89.9	1.6	2.2 ± 0.2
	C	1.59	43.7	0.72	0.70	28.8	90.9	50.6	2.5	3.5 ± 0.3
	D	1.62	43.2	0.73	0.90	71.9	204.2	120.9	1.4	1.9 ± 0.2

[a]Note that F_T is the α-ejection correction after *Ketcham et al.* [2011]; Rs equivalent radius from *Gautheron and Tassan-Got* [2010]; effective uranium content [eU] = U + 0.235 × Th ppm.

The AHe ages increase slightly with elevation from ~2.5 Ma (LI31) to ~5.4 Ma (LI24) (Table 2). The slope of the AER is $0.27^{+0.06}_{-0.04}$km/Ma (least squares regression correlation coefficient $r^2 = 0.89$; BIC value 7.5), similar to the recent AFT slope. Assuming one or two breaks in slope, the AER scenario has significantly higher BIC values of 8.6 and 10.4, respectively (Figure 7a).

In the Cuopu transect, the combined AFT and AHe data set suggests that exhumation rates have been on the order of 0.25 km/Ma since ~5 Ma.

5.2. Maoya Transect

The Maoya transect is an altitudinal profile in the granite exhumed in the footwall of the north Maoya fault (Figure 2). Five samples (CD43 to CD47) have been collected from elevations ranging between ~4200 and ~4700 m (Figure 4c). They yield AFT ages between 10.8 ± 1.3 and 16.1 ± 1.8 Ma (Table 1). The ages show a positive correlation with elevation (Figure 6b). These ages are ~5 Ma older than those of the Cuopu transect for comparable elevations. Dpar values vary between 1.62 and 2.17 μm (Table 1), slightly higher than along the Cuopu transect, suggesting slightly higher closure temperatures [*Donelick et al.*, 2005].

Table 3. Zircon Fission Track Data

Sample	Grains (*N*)	ρ_d (10^5 cm^{-2}) (Nd)	ρ_s (10^6 cm^{-2}) (Ns)	ρ_i (10^6 cm^{-2}) (*Ni*)	U (ppm)	$P(\chi^2)$ (%)	Central Age ± 1σ (Ma)
CD46	21	2.758 (4404)	12.7 (2015)	25.2 (400)	364	86.1	99.5 ± 11.5

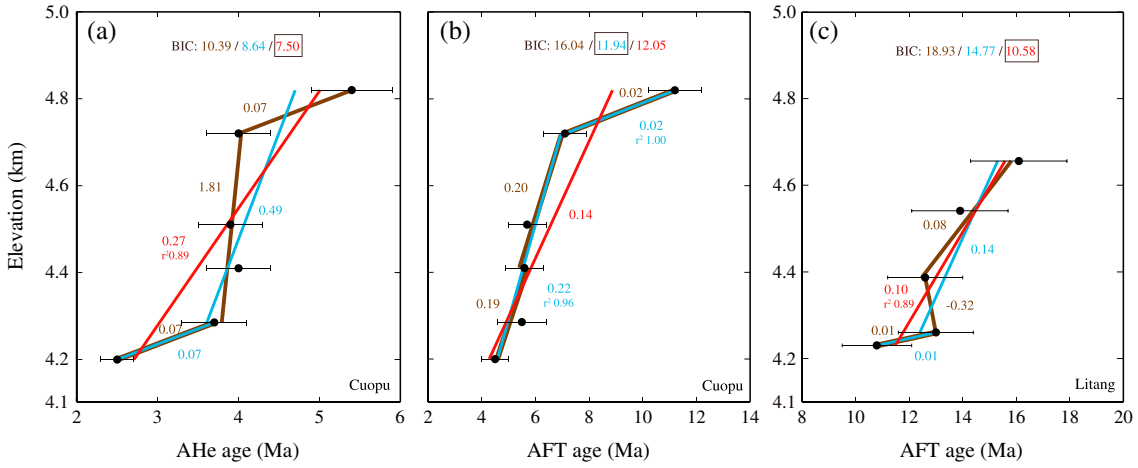

Figure 7. Age-elevation relationships of Cuopu and Maoya transects. (a) Cuopu Apatite (U-Th)/He average ages. (b) Cuopu Apatite fission track ages. (c) Maoya Apatite fission track ages. Least squares fit are calculated assuming one (red), two (blue), and three (brown) exhumation stages. For best Bayesian information criterion (BIC), correlation coefficients (R^2) and slopes are listed.

A single least squares regression yields a slope of 0.10 ± 0.03 km/Ma (mm/yr), with a correlation coefficient (r^2) of 0.89, with all samples lying within the 95% confidence interval and a BIC value of 10.6 (Figure 7c). Assuming two or three steps for the regression would lead to higher BIC values of 14.8 and 18.9, respectively, confirming that a single regression is the best fit considering the number of samples presented here.

Considering the low uranium content of most of the apatites in these samples, only CD46 has suitable grains to measure confined track lengths. CD46 has a unimodal length distribution and a mean track length of 12.6 ± 0.2 μm with a mean Dpar of 2.17 ± 0.03 μm (Table 1). This short mean track length (<13 μm) suggests prolonged residence in the partial annealing zone and relatively slow cooling in the middle Miocene.

Our AFT ages are close to those previously published. *Lai et al.* [2007] performed an altitudinal transect located 3 km west of ours: their eight AFT ages corresponding to altitudes between 4227 and 4750 m span from 10.5 ± 1.1 Ma to 23.9 ± 2.1 and show track lengths between 9.6 and 10.7 μm. Three kilometers farther west along the fault, *Wilson and Fowler* [2011] report an AFT age of 22.6 ± 3.8 Ma with track length of 11.3 ± 0.67 μm (sample 365, 4255 m).

Two of the lowermost samples yielded AHe ages (Figure 6). CD45 (~4390 m elevation) has six replicates with ages between 3.2 and 6.0 Ma, while CD46 (~4260 m elevation) has three replicates between 4.0 and 6.3 Ma (Table 2). The similar ages for these two samples separated by ~130 m of elevation difference might suggest rapid exhumation at ~5 Ma. Such rate increase has to be confirmed by thermochronological modeling taking into account both AFT and AHe results.

CD46 was the only sample with suitable zircon grains to obtain a ZFT age (Figure 6). The apparent age is 99.5 ± 11.5 Ma (Late Cretaceous). When compared with AFT ages, the ZFT age implies a slow cooling rate from within or below the ZFT partial annealing zone (~200–240°C for zircon [*Brandon et al.*, 1998]) at a rate of ~1.5°C/Ma between 100 and ~13 Ma. It would correspond to a denudation rate of ~0.05 ± 0.02 km/Ma during this time interval, assuming a paleogeothermal gradient of ~30°C/km.

In the Maoya transect, the combined ZFT, AFT, and AHe data sets show slow cooling and exhumation in the middle Miocene and possibly since the mid-Cretaceous. Between ~16 and 11 Ma, exhumation takes place at a constant rate of 0.10 ± 0.03 km/Ma, possibly increasing at ~5 Ma.

5.3. Cuola Transect

The Cuola transect follows a Yangtze tributary valley, the Cuopu river (Figure 2). Three samples (LI21 to LI23) have been collected within a limited elevation range between 3600 and 3850 m, within a 6 km horizontal distance, ~10 km downstream from the headwater catchment (Figure 3). The river has a gentle slope (~1.5°) and is not crossed by any major fault, suggesting that its incision was linked to the regional river network setting rather than to local tectonics. The samples have been collected from a porphyritic monzonitic

granite, mapped as Cretaceous (*BGMR*, 1991 (Figure 3b). Zircons extracted from sample LI21 yield a single U/Pb age population with a lower intercept age of 97.9 ± 0.8 Ma (Middle Cretaceous) (Figure 6e), close to the ~95 Ma age for another monzonitic granite ~20 km further south [*Reid et al.*, 2005a] (Figure 2).

The AFT ages vary between 13.4 ± 1.1 and 19.1 ± 1.6 Ma (Table 1). The Dpar values range between 1.54 and 1.6 μm, similar to those in the other transects. The age versus elevation has a negative correlation with the oldest age at the lowest elevation (Figure 6c). The small elevation range between the three samples (~200 m) and the large horizontal distance between them (~6 km) corresponds to a slope of less than 2°. The negative correlation should not be over interpreted as the initial relationship may have been perturbed even by a small tilting. The results suggest a mean AFT age at ~16 Ma, with a very low rate of denudation.

Two samples were analyzed for AHe. For LI21, the AHe ages range from 6.9 ± 0.6 to 14.6 ± 1.3 Ma. The ages correlate with the eU content (Table 2 and Figure 6d), which is considered as a proxy for the α-recoil damage density into the apatite grain and reflects an increase of the He retentivity. Namely, samples with higher eU tend to yield significantly older ages when they experienced slow cooling, compared to consistent ages unrelated to eU variation for fast cooling [*Flowers et al.*, 2009; *Gautheron et al.*, 2009]. Accordingly, the wide age range probably reflects a long residence time in the He partial retention zone from ~15 to ~7 Ma. LI23 has two replicates with ages at 2.0 and 4.8 Ma, suggesting a relative rapid cooling between ~5 and ~2 Ma. This attested the inception no earlier than 7 Ma as well by analogy to the samples with wide-range eU indicative of rapid cooling at Cuopu. The AHe results suggest that rapid river incision in the Cuola transect began between 7 and 2 Ma and has continued until the present.

6. Three-Dimensional Thermal-Kinematic Modeling

In order to combine the results from each thermochronometer to better constrain the recent exhumation history, the three-dimensional numerical thermal-kinematic program Pecube was run for two crustal 10 × 10 km square blocks around the Cuopu and Maoya transects (see block contours in Figures 3b and 4b), where the data are most abundant (8 AHe, 11 AFT, and 1 ZFT ages).

6.1. Model Setup

For both zones, the upper model boundary corresponds to the present-day surface topography, derived from the Shuttle Radar Topography Mission (SRTM) digital elevation model reduced to a resolution of 500 m. The lower model boundary is fixed at 50 km depth, which corresponds to the crustal thickness in this area [*Villaseñor et al.*, 2001; *Li et al.*, 2006; *Wang et al.*, 2010]. Surface temperatures were calculated using an atmospheric lapse rate of 4°C/km and a temperature at sea level of 25°C [*Bermúdez et al.*, 2011]. Other physical parameters are fixed to standard values (Table 4). Geothermal gradient and related basal temperature appear to be crucial parameters [*Glotzbach et al.*, 2011], which need to be tested to obtain an optimal result [*Bermúdez et al.*, 2011]. A high resampling ratio of 90% is set, implying a slow convergence rate, but insuring sufficient exploration of the parameter space. AHe ages are predicted assuming a 100 μm grain size [*Braun et al.*, 2012].

6.2. Inversion Results

6.2.1. Cuopu Transect

For the Cuopu transect, we used Pecube to model a two-stage scenario, as suggested by the AER of AHe and AFT. The model runs for 20 Ma, with a transition time T between the two phases varying from 20 to 0 Ma, with exhumation rates during the first phase (E1) and the second phase (E2) varying from 0 to 2 km/Ma (Table 4). The relief factor (R) can vary between 0 and 1, and the basal temperature between 600 and 800°C (Table 4). The relief factor R is defined as the ratio between the initial (h_1) and present-day relief (h_2): $R = h_1/h_2$ [*Valla et al.*, 2010].

The inversion result shows that such a two-stage history is well constrained. Denudation rate E1 during the first stage ranges from 0.005 to 0.5 km/Ma, with a high maximum probability at a rate approaching zero (Figure 8a), consistent with the 0.02 km/Ma deduced from AER for AFT (Figure 7b). The onset time of exhumation (T) is also well constrained, ranging from 3 to 6 Ma, with a maximum probability at 5.3 ± 0.4 Ma (Figure 8a), similar to that deduced from AFT AER (Figure 6). The recent exhumation rate is fast, ranging between 0.8 and 1.2 km/Ma, with a maximum probability at a rate of 0.99 ± 0.04 km/Ma (Figure 8a). The relief

Table 4. Pecube Thermal and Mechanical Parameter Values Common and Simulation Parameters Specific for the Cuopu and Maoya Transects[a]

Thermal Parameters		Value	Reference	Plate Flexural Parameters	Value	Reference	
Crustal thickness		50 km	*Wang et al.* [2010] and *Li et al.* [2006]	Crustal density	2700 kg m^{-3}	*Valla et al.* [2010]	
Thermal diffusivity		25 km^2 Ma^{-1}	*Braun and Robert* [2005]	Mantle density	3200 kg m^{-3}	*Valla et al.* [2010]	
Temperature at sea level		25°C	*Bermúdez et al.* [2011]	Young's modulus	1.10^{11} Pa		
Atmospheric lapse rate		4°C km^{-1}	*Bermúdez et al.* [2011]	Poisson ratio	0.25		
Crustal heat production		10°C Ma^{-1}		Equivalent elastic thickness	28.8 km		
Transect	**Scenarios**	**Parameter Range**	**Annotation**		**Dimension**	**Misfit**	**Number of Models**
Cuopu	Constant exhumation	*T*: 0–20 Ma	Onset time		4	0.47	10100
		E: 0–2 km/Ma	Denudation rate				
		R: 0–1	Relief factor				
		600–800°C	Basal temperature				
	Two-stage exhumation (run over 20 Ma)	***T*:0–20 Ma**	**Transition time**		**5**	**0.439**	**10100**
		***E*$_1$: 0–2 km/Ma**	**Denudation rate of the first phase**				
		***E*$_2$: 0–2 km/Ma**	**Denudation rate of the second phase**				
		***R*: 0-1**	**Relief factor**				
		600 - 800°C	**Basal temperature**				
Maoya	Constant exhumation	*T*: 0–100 Ma	Onset time		3	0.33	10100
		E: 0–2 km/Ma	Denudation rate				
		R: 0-1	Relief factor				
		723°C	Fixed basal temperature				
	Two-stage exhumation (run over 100 Ma)	***T*:0–100 Ma**	**Transition time**		**4**	**0.227**	**10100**
		***E*$_1$: 0–2 km/Ma**	**Denudation rate of the first phase**				
		***E*$_2$: 0–2 km/Ma**	**Denudation rate of the second phase**				
		***R*: 0-1**	**Relief factor**				
		723°C	**Fixed basal temperature**				
	Three-stage exhumation (run over 100 Ma)	T_1:8–100 Ma	Transition time between first and second phase		7	0.28	10100
		T_2:0–8 Ma	Transition time between second and third phase				
		E_1: 0–2 km/Ma	Denudation rate of the first phase				
		E_2: 0–2 km/Ma	Denudation rate of the second phase				
		E3: 0–2 km/Ma	Denudation rate of the third phase				
		R_{1-2}: 0-1	Relief factor of the first phase				
		R_3: 0-1	Relief factor of the second phase				
		723°C	Fixed basal temperature				

[a]Note the optimal scenarios with lowest misfit for each transect are in bold.

change (*R*) and the basal temperature are less well constrained with a more continuous probability distribution, with a maximum probability for the relief-ratio (*R*) at 0.65 ± 0.06 and the basal temperature at 723 ± 18°C (equivalent to geothermal gradient of 32°C/km) (Figure 8c). Such basal temperature and corresponding geothermal gradient yield a high recent exhumation rate, three times higher than the 0.27 km/Ma deduced from the AER for AHe. But the AER rate would not be sustainable until present day, as its *y* intercept, which corresponds to the present-day depth of the AHe closure temperature isotherm if the exhumation rate was constant until present day, is too shallow [*Reiners and Brandon*, 2006]. For the Cuopu transect, the *y* intercept is 3.6 km above see level, only 0.9 km below the present-day mean elevation (~4.5 km) (Figure 6a). If we assume

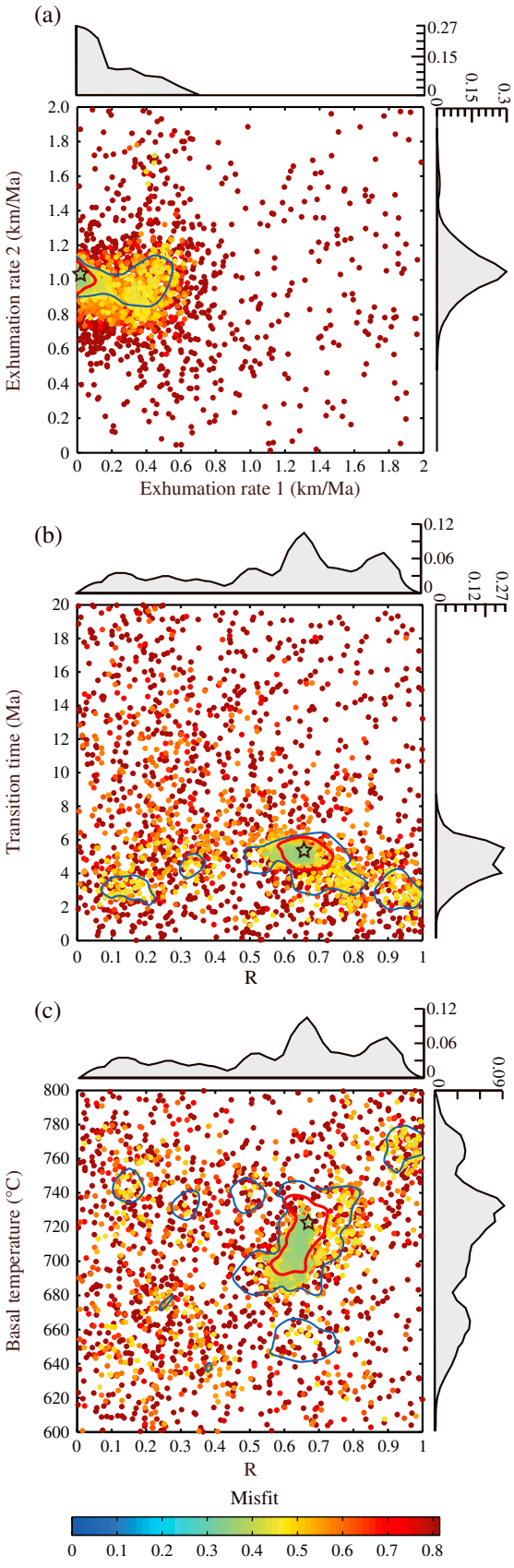

a steady geothermal gradient of ~32°C/km, a closure temperature of AHe ~70°C, and surface temperature of 10°C, the expected closure depth for AHe is ~2 km beneath present-day mean elevation (2500 m above sea level (asl)). The fact that the observed closure depth is 1.1 km higher than the expected one attests to an increase of the exhumation rate from the youngest mean AHe age (ca. 2.5 Ma) to the present. It implies a higher exhumation rate since 5.3 Ma than the apparent exhumation rate deduced from the AHe AER.

6.2.2. Maoya Transect

For the Maoya transect, the inferred scenarios span a much longer time period in order to take into account the ~99 Ma ZFT age. A two-phase scenario has been defined, starting at 100 Ma, with four variable parameters (Table 4): (1) transition time between first and second phase (T_1: 0–100 Ma), (2) denudation rate of the first phase (E_1 ranging between 0 and 2 km/Ma), (3) denudation rate of the second phase (E_2 varying within the same range 0-2 km/Ma), and (4) mean relief factor for both first and second phases (R_{1-2}: 0–1). The basal temperature is fixed at 723°C according to the Cuopu transect inversion.

The inversion results constrain these parameters (Figure 9). The preferred solution shows a first quiet phase with a slow exhumation rate ($E_1 = 0.03 \pm 0.03$ km/Ma) sustained from 100 Ma to $T = 6.6 \pm 0.5$ Ma (range from 4.6 to 8.5 Ma), followed by an active period with a more rapid exhumation rate $E_2 = 0.59 \pm 0.03$ km/Ma since T (Figure 9). The maximum probability for the relief-ratio parameter R_{1-2} is 0.56 ± 0.5. This scenario generates predicted ages that fit all measured ages within the 95% confidence interval or the error limit (Figure 6b). The slow first phase exhumation rate ($E_1 = 0.03 \pm 0.03$ km/Ma) is consistent with the $0.1 + 0.09 - 0.03$ km/Ma deduced from the AFT AER (Figure 6b).

Figure 8. Pecube inversion results for AHe and AFT data of Cuopu transect. Two-dimensional scatterplots of inversion results. Color points correspond to misfit values (common scale), 1-D probability density functions appear along the axes. The optimal solution is shown by a star with 2σ (blue) and 1σ (red) confidence contours. (a) Exhumation rate of the first phase (E_1) versus exhumation rate of the second phase (E_2). (b) Relief change (R) versus timing of initiation of the second exhumation phase. (c) Relief change (R) versus temperature at 50 km depth.

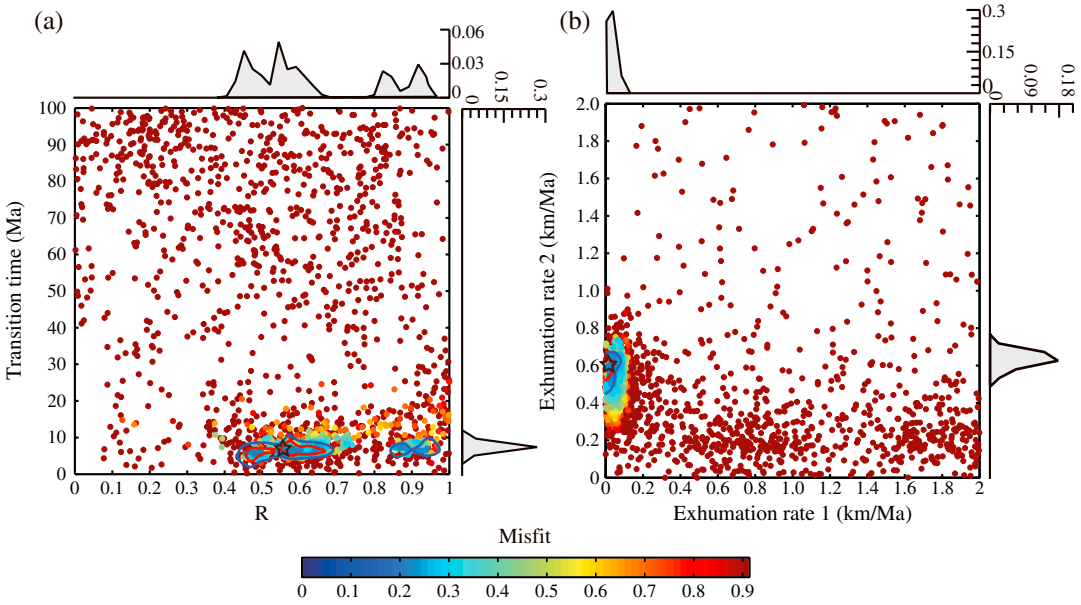

Figure 9. Pecube inversion results for AHe, AFT, and ZFT data of Maoya transect. Two-dimensional scatterplots of inversion results. Color points correspond to misfit values (common scale), 1-D probability density functions appear along the axes. The optimal solution is shown by a star, with 2σ (blue) and 1σ (red) confidence contours. (a) Relief change (*R*) versus timing of initiation of the second exhumation phase (T_2). (b) Exhumation rate of the first phase (E_1) versus exhumation rate of the second phase (E_2).

7. Discussion

7.1. Kinematics of the Litang Fault System

We combine structural mapping with thermochronologic data in order to infer the timing of fault activity and the rate of footwall exhumation. We use two elevation profiles (Maoya and Cuopu) to constrain the exhumation history by Pecube models, which allow discussion of the Neogene kinematics in the frame SE Tibet active deformation.

7.1.1. Exumation History of the Litang Fault System

According to our FT and AHe ages, the Cuopu and Maoya transects show evidence for rapid cooling and hence exhumation during the Neogene. For the Maoya profile, our results show a tectonic quiet period with almost no exhumation since at least 100 Ma until ~6 Ma, followed by a sharp increase of the exhumation rate to ~0.6 km/Ma (Figure 10), together with a relief increase. For the Cuopu profile, the most recent rapid exhumation phase has been quantified with a higher rate of ~1 km/Ma since ~5 Ma (Figure 10). Such rates would correspond to a total exhumation of 3.9 km along the Maoya profile since 6 Ma and of 5.2 km along the Cuopu profile since 5 Ma. The exhumation increase from east (Maoya) to west (Cuopu) is compatible with the increase of the ranges maximum elevation from east (~5000 m) to west (~5800 m).

The minimum total vertical offset on the faults is the sum of the elevation difference between the highest relief in the footwalls and the top of the hanging wall basins with the thickness of the detrital deposits found in these basins. The altitude difference amounts to ~1000 m in Maoya and ~1700 m in Cuopu. The basin thickness is unknown. The minimum estimation of the thickness is 300–400 m, as observed for the Jawa basin [*Zhou et al.*, 2005]. In that case, the total vertical offsets are 1400 m in Maoya and 2100 m in Cuopu, far less than the exhumation inferred from Pecube thermal modeling (respectively, 3900 m and 5200 m). A maximum estimation of the basin thickness could be ~2000 m, as observed for the basin at the foot of the Diancang Shan normal fault (Figure 1) [*Leloup et al.*, 1993]. In that case, the total vertical offsets would be 3000 m in Maoya and 3700 m in Cuopu, still less than the exhumation inferred from Pecube thermal modeling. This implies that a significant portion of the footwalls have been eroded away without being trapped in the basins, or that the Pecube estimates are too high. Such overestimation could be due to poor constraints on the basal temperature and thermal gradient.

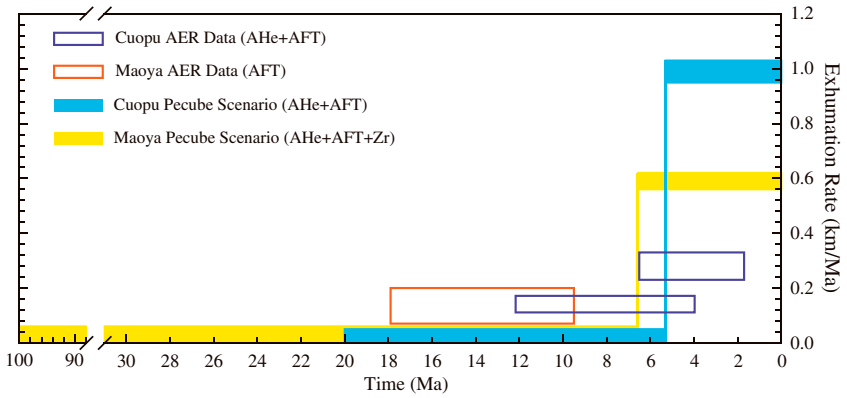

Figure 10. Exhumation evolution through time from thermal-kinematic model inversion for the Litang Fault. The dark blue and orange boxes indicate quantitative description of data age fields and apparent exhumation rates deduced from each AER for the two transects; azure and yellow boxes indicate the optimal scenario with different thermometers; boxes indicate 1σ analytical uncertainty.

We interpret the rapid increase in the exhumation rate between 7 and 5 Ma as the activation of the normal motion component of Litang fault system. In Maoya, *Xu et al.* [2005] estimated a vertical rate of 1.8 ± 0.6 mm/yr since ~10 ka, but our own estimation is ~0.6 mm/yr since ~20 ka (Marie-Luce Chevalier, personal communication). The latter rate is identical with the one we deduce from the Pecube model (0.59 ± 0.03 mm/yr), providing independent support for the exhumation rate of the Pecube model, and suggesting a steady state exhumation since ~6.6 Ma.

7.1.2. Relationships Between Left-Lateral and Normal Component of Motion of the Litang Fault System

A strike-slip component of motion has been previously mapped along most segments of the Litang fault system from left-lateral seismic surface ruptures and morphologic marker offsets, such as alluvial fans [*Xu et al.*, 2005]. Indeed, well-preserved left-lateral surface ruptures, possibly meter-scale coseismic gully offsets, are very clear for the Litang and Dewu faults (Figure 5d), but larger cumulative offsets are unclear and the strike-slip faults are hard to map away from the surface ruptures. On the contrary, the North Cuopu and North Maoya faults morphology shows pure normal motion since at least ~20 ka (Figures 3 and 4). Morphological left-lateral offsets are not observed for these fault segments, but we observe long-term left-lateral offset of granites and Triassic sediments between 6 and 11 km (Figures 2–4). The North Maoya fault left-laterally offsets by 14 km the western edge of Paleozoic rocks overlain by N-S Eocene basins (Figures 2 and 5). The Eocene basins are in fact poorly dated but their offset implies that the left-lateral motion is Cenozoic. Such long term offsets suggest that left-lateral motion has occurred prior to the present-day pure normal motion observed for the Cuopu and Maoya faults. To the southeast, the South Jawa fault plane shows two sets of slickenside striations, a left-lateral one with a pitch of 20°W and a normal one with a pitch of 90°, the latter clearly cutting the left-lateral striation (Figure 5f). These crosscutting relationships also show that left-lateral motion have occurred prior to the normal motion.

Our observations imply that the Litang fault system is a transtensive left-lateral fault system, with variation of extensive and strike-slip components of motion in time depending on the fault segments. However, all fault segments show vertical motion together with larger left-lateral ones, either coeval as for the Litang and Dewu fault segments seismic ruptures (Figures 5c and 5d), or successive as for the Cuopu, Maoya, and Jawa fault segments (Figures 5e and 5f). It suggests that normal motion takes place together with a left-lateral component. The North Maoya and the South Jawa faults (azimuth ~N110) are slightly oblique to the Litang and Dewu fault segments (azimuth ~N130) (Figure 2), such as they may act as releasing bends and absorbing part of the left-lateral motion. In that case, the onset of the vertical motion of the fault system would be coeval to the initiation of the overall fault system.

Our thermochronology study implies that normal motion on the Cuopu and North Maoya faults initiated between 5 and 7 Ma (Figure 10). Using such estimation and the long term left-lateral offsets, between 6 and 14 km, the mean horizontal rate is between 0.9 and 2.8 mm/yr.

7.1.3. Present-Day Regional Kinematics

The GPS velocity field of the Litang Plateau, with respect to Eurasia (Figure 1), shows southeastward motion at a rate of ~15 mm/yr with a counterclockwise rotation around a pole located close to the eastern Himalaya syntaxis [e.g., *Zhang et al.*, 2004; *Gan et al.*, 2007; *Copley*, 2008]. North of the XSHF, motions with respect to Eurasia are slower, and convergence across the Longmen Shan is negligible (Figure 1). Despite this low GPS-based convergence rate, a devastating magnitude 7.9 earthquake with a large shortening component occurred in 2008 along the Longmen Shan causing more than 80000 casualties [e.g., *Xu et al.*, 2009; *de Michele et al.*, 2010; *E. Wang et al.*, 2012; *Oskin*, 2012]. This event illustrated that GPS measurements alone are not sufficient to infer seismic hazard and that the mapping and study of major fault zones stay fundamental to understand recent deformations.

Northeast of the Litang fault system one station moves ~18 mm/yr in the N132 direction, while two stations southwest of the fault moves ~18 mm/yr in the N120 direction and ~19 mm/yr in the N134 direction respectively (Figure 1). Taken at face value these velocities would, respectively, imply a 3.8 mm/yr convergence and a 1.3 mm/yr left-lateral/extension across the Litang fault that strikes ~N130. Such estimates are not consistent with our conclusion that the motion on the fault is normal with a left-lateral component. We conclude that there are too few GPS stations and that the uncertainties are too large for these estimates to be significant. The GPS signal is thus probably not adequately describing the long-term deformation of the Litang fault system.

7.2. Regional Incision

Since the Miocene SE Tibet has been dissected by regressive erosion of the main rivers flowing out of the plateau [e.g., *Clark et al.*, 2005; *Liu-Zeng et al.*, 2008]. Previous thermochronological studies have established that the eastern Tibetan Plateau has been incised rapidly between 9 and 13 Ma by the Jinsha/Yangtze rivers and its two main tributaries, the Dadu and Yalong rivers [*Xu and Kamp*, 2000; *Clark et al.*, 2005; *Ouimet et al.*, 2010]. Such middle Miocene initiation of major river rapid incision has been used as a proxy for the uplift of southeastern Tibet, inferred to begin at ~13 Ma [ibidem]. However, a recent study has suggested an earlier onset of incision, which could have occurred since the Early Miocene (~15–22 Ma) along a Yangtze tributary incising the south end of the Daocheng pluton (Figure 2) [*Tian et al.*, 2014]. An early Miocene onset of river incision is consistent with the rate of sedimentation in the South China Sea being maximal at that time (24–11 Ma) [*Clift*, 2006].

Along the Cuopu river a second order Yangtze tributary, our results, along the Cuola transect, show that after a very low rate of denudation since ~16 Ma, beginning of rapid cooling took place between 7 and 2 Ma ago (Figure 6c), which we interpret to be related to the beginning of the Cuopu river incision. This result gives an estimate for the time at which the regressive incision reached that part of SE Tibet. Given the various time estimates it seems that the available thermochronologic data set is not yet dense enough to image the propagation of the regressive erosion during the Miocene and decipher between the various mechanisms proposed to yield to plateau uplift and river incision.

7.3. Regional Cenozoic Kinematics

As described in the geological setting section (section 2.2), the Litang fault system is located between the left-lateral XianShuiHe fault (XSHF) to the north and the right-lateral Zhongdian fault to the south that connects with the Red River fault through the Lijiang pull-apart (Figure 1). Most geochronologic data suggest that the XSHF system is active since at least 10–12 Ma [*Roger et al.*, 1995; *Wang et al.*, 2009; *Li and Zhang*, 2013] and propagated across the Jinhe-Qinghe thrust system toward the Xiaojiang transtensive fault system at ~5 Ma [*S. Wang et al.*, 2012]. We infer the onset age of the right-lateral Zhongdian fault to be contemporaneous with the exhumation of the Diancang Shan range bounding to the south the Lijiang pull-apart (Figure 1), which started at ~5 Ma [*Leloup et al.*, 1993]. Farther southeast, the activation of the dextral Red River Fault has been estimated as taking place at 10–11 Ma [*Leloup et al.*, 2001]. At the southeast end of the fault, age of onset of folding in the Tonkin gulf absorbing the right-lateral motion, initially estimated at ~5 Ma [*Replumaz et al.*, 2001; *Schoenbohm et al.*, 2006] was recently reestimated at 8–9 Ma [*Fyhn and Phach*, 2015].

Our data show that the Litang fault system initiated between 7 and 5 Ma (Figure 10). This appears to be contemporaneous to the activation of the Zhongdian fault and the Lijiang pull-apart as well with the

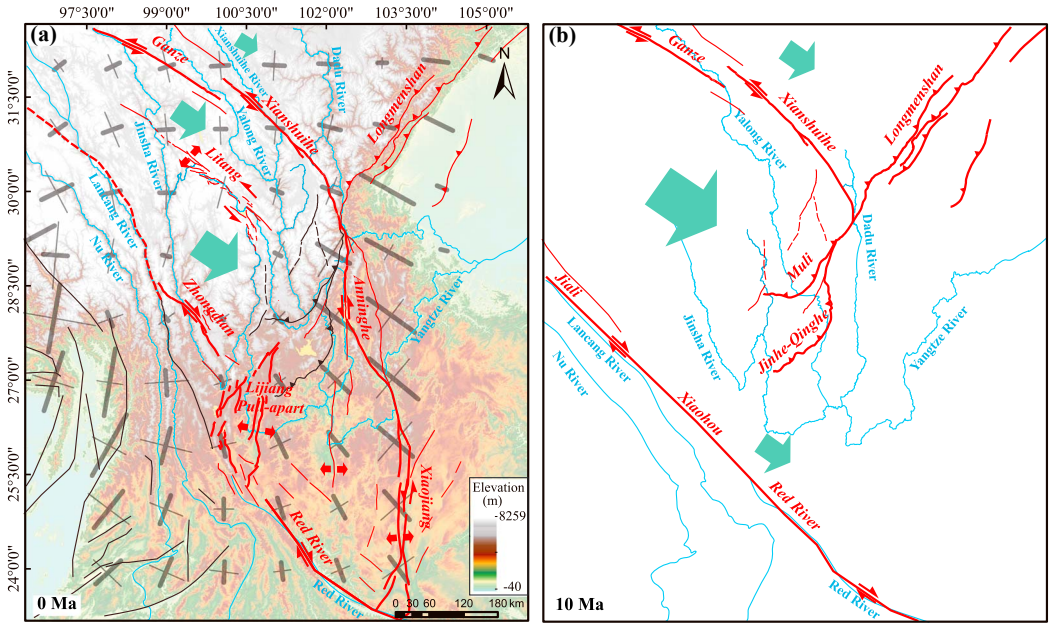

Figure 11. Late Cenozoic evolution of Southeastern Tibet Plateau. Active faults appear in red while red arrows indicate relative motions, and blue arrows indicate qualitative block motion with respect to Indochina. (a) Present-day fault network. The color background corresponds to the topography. The grey crosses correspond to strain (second invariant of the horizontal strain rate tensor) predicted from a channel flow numerical model corresponding to the GPS data, with thick and thin lines being the direction of compression and extension, respectively (from Figure 13 of *Copley*, 2008). The Litang, Zhongdian, and Anninghe-Xiaojiang faults initiated between 7 and 5 Ma (b) pre-Pliocene fault network (~10 Ma). Lateral motion of the XSHF was absorbed by shortening along the Muli and Jinhe-Qinghe thrust systems, in the prolongation of the Longmen Shan.

southeastward propagation of the XSHF along the Xiaojiang fault system (Figure 11a). This suggests that a major fault reorganization occurred in SE Tibet at 7–5 Ma. Prior to that reorganization, between ~12 and ~5 Ma, left-lateral motion of the XSHF was absorbed by shortening on the Muli and Jinhe-Qinghe thrust systems (Figure 11b), while right-lateral motion along the Red River fault was absorbed by shortening in the Tonkin Gulf. After the fault reorganization and the activation of the Litang fault, the XSHF propagated toward the south and started to bend the Red River fault [*Schoenbohm et al.*, 2006], while the right-lateral Zhongdian fault connected to the Red River through the Lijiang pull-apart (Figure 11a). In this new situation three zones are affected by local extension: ~WNW-ESE extension in the Lijiang pull-apart, E-W extension in the Xiaojiang fault system and NE-SW extension across the Litang fault system (Figure 11a).

In our favored scenario, the Zhongdian and the Xianshuihe strike-slip faults allow the sliding to the east of a wide continental block with the Litang fault system accommodating differential motion within this block (Figure 11a). Such lateral motion guided by strike-slip faults is in agreement with the hidden plate-tectonic model [e.g., *Meyer et al.*, 1998; *Tapponnier et al.*, 2001; *Replumaz and Tapponnier*, 2003], which enlighten the role of strike-slip faults. In that model because of the northward migration of the Indian indenter, the eastward extrusion of Indochina along the left-lateral Ailao Shan - Red River shear zone ends in the middle Miocene (~16 Ma) and if followed by the activation of the right-lateral RRF system linking the Jiali, Xiaohou, and Red River *s.s.* faults (Figure 11b) [e.g., *Armijo et al.*, 1989; *Tapponnier et al.*, 1986; *Leloup et al.*, 1995; *Lacassin et al.*, 1997]. Similarly, the activation of the right-lateral Zhongdian fault is linked with the northward propagation of the Indian indenter east corner, which overtook the position of the Xiaohou segment of the RRF between 10 and 5 Ma so that a new fault initiates farther north (Figure 11a), [e.g., *Replumaz and Tapponnier*, 2003]. Before the Pliocene lateral motion of the XSHF was absorbed by shortening along the Muli thrust system (Figure 11b). Such successive deformation phases initiated by the northward migration of the indenter are a major aspect of the hidden plate-tectonic model.

Table 5. Li21b (U-Th)/Pb Data

Analysis_#	Pb (ppm)	Th (ppm)	U (ppm)	Th/U	Pb207/U235	Pb207/U235	Pb206/U238	Pb206/U238	Rho	Pb206/U238	Pb206/U238
35060913c	43	750	2902	0.26	0.1008	0.0041	0.01512	0.00057	0.93	96.7	3.7
36060913c	12	210	794	0.26	0.1041	0.0044	0.01547	0.00060	0.93	99.0	3.8
37060913c	40	976	2567	0.38	0.1005	0.0039	0.01502	0.00057	0.97	96.1	3.7
38060913c	25	289	1683	0.17	0.1031	0.0041	0.01539	0.00060	0.99	98.5	3.8
39060913c	10	201	627	0.32	0.1120	0.0049	0.01594	0.00060	0.86	101.9	3.9
40060913c	21	279	1394	0.20	0.1055	0.0042	0.01595	0.00060	0.94	102.0	3.9
41060913c	45	808	2924	0.28	0.1039	0.0040	0.01571	0.00060	0.99	100.5	3.8
42060913c	13	43	84	0.51	1.3576	0.0571	0.14422	0.00555	0.92	869	31
45060913c	42	555	2827	0.20	0.1026	0.0040	0.01543	0.00060	0.99	98.7	3.8
46060913c	38	430	2635	0.16	0.1005	0.0039	0.01502	0.00057	0.98	96.1	3.6
47060913c	12	444	684	0.65	0.1057	0.0049	0.01506	0.00057	0.82	96.4	3.7
48060913c	32	262	2207	0.12	0.1086	0.0042	0.01531	0.00057	0.96	97.9	3.7
49060913c	55	897	3723	0.24	0.1009	0.0039	0.01517	0.00057	0.98	97.1	3.7
50060913c	28	475	1849	0.26	0.1004	0.0040	0.01525	0.00057	0.95	97.6	3.7
51060913c	10	142	714	0.20	0.0994	0.0042	0.01512	0.00057	0.89	96.8	3.7
52060913c	26	705	1650	0.43	0.1088	0.0043	0.01536	0.00057	0.94	98.3	3.7
55060913c	28	415	1872	0.22	0.1031	0.0041	0.01550	0.00060	0.99	99.1	3.8
56060913c	49	653	3361	0.19	0.1012	0.0039	0.01520	0.00057	0.97	97.3	3.7
57060913c	10	328	591	0.55	0.1138	0.0058	0.01536	0.00060	0.77	98.3	3.8
58060913c	54	693	3705	0.19	0.1021	0.0039	0.01518	0.00057	0.98	97.1	3.7
59060913c	42	1097	2659	0.41	0.1018	0.0040	0.01530	0.00057	0.94	97.9	3.7
60060913c	12	82	864	0.09	0.0990	0.0041	0.01497	0.00057	0.91	95.8	3.6
61060913c	20	184	1371	0.13	0.1118	0.0044	0.01519	0.00057	0.94	97.2	3.7
62060913c	18	134	1259	0.11	0.1135	0.0045	0.01502	0.00057	0.96	96.1	3.6
65060913c	52	479	3618	0.13	0.1019	0.0039	0.01522	0.00057	0.98	97.4	3.7
66060913c	50	745	3453	0.22	0.0983	0.0038	0.01473	0.00057	0.98	94.3	3.5
67060913c	15	322	968	0.33	0.1005	0.0041	0.01513	0.00057	0.92	96.8	3.6
68060913c	42	393	2918	0.13	0.1013	0.0039	0.01507	0.00057	0.98	96.4	3.6
69060913c	40	435	2665	0.16	0.1037	0.0041	0.01553	0.00060	0.98	99.4	3.7
70060913c	58	636	3788	0.17	0.1060	0.0041	0.01605	0.00060	0.97	102.6	3.8
71060913c	22	332	1481	0.22	0.0986	0.0039	0.01492	0.00057	0.96	95.5	3.6
72060913c	41	314	2856	0.11	0.1042	0.0041	0.01511	0.00057	0.97	96.7	3.6

Uplift of the eastern Tibetan Plateau resulting from outward lower crustal viscous flow from the plateau center would be unrelated to thrust and strike-slip faulting [e.g., *Clark and Royden*, 2000]. Because such flow is a continuous process through time it could not induce successive phases of deformation, in contradiction within our scenario (Figure 11). Nevertheless, it has also been proposed that two different mechanisms may have succeeded through time and that extrusion tectonics along the right-lateral Red River fault was succeeded by propagation of the Tibetan Plateau through lower channel flow since the Pliocene (~5 Ma) [*Schoenbohm et al.*, 2006]. In that case, the XSHF connecting to the Xiaojiang fault system has been interpreted as following the viscous lower crust flow from the center of the plateau to its edges around the Sichuan craton [*Schoenbohm et al.*, 2006]. For this recent deformation phase, numerical model that produces a velocity field comparable to the GPS data predict extension perpendicular to the flow near the edge of the plateau, as well as in the lowlands where the flow spreads out (Figure 11a) [*Copley*, 2008]. Our study shows that extension in SE Tibet is observed both along the Litang and Xiaojiang fault systems, and in the Lijiang pull-apart. Some segments of the Litang fault system, like the Maoya fault, are indeed more or less perpendicular to the flow and parallel to the direction of extension in numerical model of such flow (Figure 11a). However, the trend of the Litang fault system (N130°) is oblique to that flow. Out of the high plateau, some fault segments of the Lijiang pull-apart are more or less parallel to the divergent flow outward of the high Plateau, but again the trend of the fault is oblique to the flow. On the contrary, the extension observed in the Xiaojiang fault system is clearly oblique to the flow and is not in agreement with the model. Furthermore, extension is not spread out as predicted by the homogeneity of the flow but concentrated along the strike-slip faults.

8. Conclusion

In this paper, we constrain the exhumation history of the Litang fault system with AHe, AFT, and ZFT thermochronology elevation transects within granitic ranges. In the footwall of the North Maoya fault

segment, we show that a tectonic quiet period, a slow denudation rate of 0.03 km/Ma, was sustained since at least 100 Ma, until a sudden increase of exhumation and relief at 6.6 ± 0.5 Ma with a rapid exhumation rate of 0.59 ± 0.03 km/Ma. In the footwall of the North Cuopu fault segment, comparable recent rapid exhumation has been constrained, with an increase of the exhumation rate from 0.005 km/Ma to 0.99 ± 0.04 km/Ma at 5.3 ± 0.4 Ma.

We interpret the rapid increase in the exhumation rate between 5 and 7 Ma as corresponding to the activation of the left-lateral/normal Litang fault system. Such timing appears to correspond to a regional fault kinematics reorganization in SE Tibet together with the propagation of the Xianshuihe fault along the Xiaojiang transtensive fault system and the activation of the right-lateral Zhongdian strike-slip fault connecting with the RRF through the Lijiang pull-apart (Figure 11a). Such strike-slip faults allow the sliding to the east of a wide continental block, with the Litang fault system accommodating differential motion between two parts of the block (Figure 11a). This implies that the regional evolution is guided by the strike-slip faults, with different phases of deformation, which appears more in agreement with the hidden plate-tectonic model rather than with the "lower channel flow" model.

Acknowledgments

This work has been supported by the National Special Project on the Tibetan Plateau of the Geological Survey of China (1212011121261 and 1212010610103), the China Scholarship Council Funds, and the Labex OSUG@2020 (Investissements d'avenir—ANR10 LABX56). Campus France PHC XU GUANGQI 2012N° 27928YC and PHC CAI YUANPEI N° 27968UC (French ministry of foreign affairs) were also used as well as support from the SYSTER (INSU-CNRS) program. Elizabeth Hardwick, Audrey Margirier, and Mélanie Noury are thanked for samples preparation. Rosella Pinna-Jamme and Eric Douville are thanked for (U-Th)/He dating. Christoph Glotzbach is thanked for providing the BIC code. Jean Braun is warmly thanked for providing the Pecube code and constructive comments. Both codes used in this paper are published and available on demand to the authors. All protocols are published and referenced in the text. All data used in this paper are included in the paper (Tables 1–5).

References

Akaike, H. (1974), A new look at the statistical model identification, *Automat. Contr. IEEE Trans.*, *19*(6), 716–723.

Allen, C. R., L. Zhuoli, Q. Hong, W. Xueze, Z. Huawei, and H. Weishi (1991), Field study of a highly active fault zone: The Xianshuihe fault of southwestern China, *Geol. Soc. Am. Bull.*, *103*(9), 1178–1199.

Armijo, R., P. Tapponnier, and T. Han (1989), Late Cenozoic right-lateral strike-slip faulting in southern Tibet, *J. Geophys. Res.*, *94*(B3), 2787–2838, doi:10.1029/JB094iB03p02787.

Arne, D., B. Worley, C. Wilson, S. F. Chen, D. Foster, L. Zhili, L. Shugen, and P. H. G. M. Dirks (1997), Differential exhumation in response to episodic thrusting along the eastern margin of the Tibetan Plateau, *Tectonophysics*, *280*(3–4), 239–256.

Barbarand, J., A. Carter, I. Wood, and T. Hurford (2003), Compositional and structural control of fission-track annealing in apatite, *Chem. Geol.*, *198*(1–2), 107–137.

Beaumont, C., R. A. Jamieson, M. H. Nguyen, and S. Medvedev (2004), Crustal channel flows: 1. Numerical models with applications to the tectonics of the Himalayan-Tibetan orogen, *J. Geophys. Res.*, *109*, B06406, doi:10.1029/2003JB002809.

Bermúdez, M. A., P. van der Beek, and M. Bernet (2011), Asynchronous Miocene–Pliocene exhumation of the central Venezuelan Andes, *Geology*, *39*(2), 139–142.

Brandon, M. T., M. K. Roden-Tice, and J. I. Garver (1998), Late Cenozoic exhumation of the Cascadia accretionary wedge in the Olympic Mountains, northwest Washington State, *Geol. Soc. Am. Bull.*, *110*(8), 985–1009.

Braun, J. (2003), Pecube: A new finite-element code to solve the 3D heat transport equation including the effects of a time-varying, finite amplitude surface topography, *Comput. Geosci.*, *29*(6), 787–794.

Braun, J., and X. Robert (2005), Constraints on the rate of post-orogenic erosional decay from low-temperature thermochronological data: Application to the Dabie Shan, China, *Earth Surf. Process. Landf.*, *30*(9), 1203–1225.

Braun, J., P. van der Beek, P. Valla, X. Robert, F. Herman, C. Glotzbach, V. Pedersen, C. Perry, T. Simon-Labric, and C. Prigent (2012), Quantifying rates of landscape evolution and tectonic processes by thermochronology and numerical modeling of crustal heat transport using PECUBE, *Tectonophysics*, *524–525*, 1–28.

Brown, R. W., M. A. Summerfield, and A. J. Gleadow (1994), Apatite fission track analysis: Its potential for the estimation of denudation rates and implications for models of long-term landscape development, in *Process Models and Theoretical Geomorphology*, edited by M. J. Kirby, pp. 23–53, Wiley, Chichester, U. K.

Bureau of Geology and Mineral Resources (BGMR) (1991), *Regional Geology of Sichuan Province*, Geological House, Beijing.

Carlson, W. D., R. A. Donelick, and R. A. Ketcham (1999), Variability of apatite fission-track annealing kinetics; I, Experimental results, *Am. Mineral.*, *84*(9), 1213–1223.

Chengdu Institute of Geology and Mineral Resources (CIGMR) (2004), *Geological Map of Tibetan Plateau and Its Vicinity*, Chengdu Map Press, Chengdu.

Clark, M. K., and L. H. Royden (2000), Topographic ooze: Building the eastern margin of Tibet by lower crustal flow, *Geology*, *28*(8), 703–706.

Clark, M. K., M. A. House, L. H. Royden, K. X. Whipple, B. C. Burchfiel, X. Zhang, and W. Tang (2005), Late Cenozoic uplift of southeastern Tibet, *Geology*, *33*(6), 525–528.

Clark, M. K., L. H. Royden, K. X. Whipple, B. C. Burchfiel, X. Zhang, and W. Tang (2006), Use of a regional, relict landscape to measure vertical deformation of the eastern Tibetan Plateau, *J. Geophys. Res.*, *111*, F03002, doi:10.1029/2005JF000294.

Clift, P. D. (2006), Controls on the erosion of Cenozoic Asia and the flux of clastic sediment to the ocean, *Earth Planet. Sci. Lett.*, *241*(3–4), 571–580.

Copley, A. (2008), Kinematics and dynamics of the southeastern margin of the Tibetan Plateau, *Geophys. J. Int.*, *174*(3), 1081–1100.

De Michele, M., D. Raucoules, J. De Sigoyer, M. Pubellier, and N. Chamot-Rooke (2010), Three-dimensional surface displacement of the 2008 May 12 Sichuan earthquake (China) derived from Synthetic Aperture Radar: Evidence for rupture on a blind thrust M. de Michele et al. 3D surface displacement of Sichuan earthquake, *Geophys. J. Int.*, *183*(3), 1097–1103.

de Sigoyer, J., O. Vanderhaeghe, S. Duchêne, and A. Billerot (2014), Generation and emplacement of Triassic granitoids within the Songpan Ganze accretionary-orogenic wedge in a context of slab retreat accommodated by tear faulting, Eastern Tibetan Plateau, China, *J. Asian Earth Sci.*, *88*, 192–216.

Donelick, R. A., P. B. O'Sullivan, and R. A. Ketcham (2005), Apatite fission-track analysis, *Rev. Mineral. Geochem.*, *58*(1), 49–94.

Farley, K. A. (2000), Helium diffusion from apatite: General behavior as illustrated by Durango fluorapatite, *J. Geophys. Res.*, *105*(B2), 2903–2914, doi:10.1029/1999JB900348.

Fillon, C., C. Gautheron, and P. van der Beek (2013), Oligocene–Miocene burial and exhumation of the Southern Pyrenean foreland quantified by low-temperature thermochronology, *J. Geol. Soc.*, *170*(1), 67–77.

Fitzgerald, P. G., R. B. Sorkhabi, T. F. Redfield, and E. Stump (1995), Uplift and denudation of the central Alaska Range: A case study in the use of apatite fission track thermochronology to determine absolute uplift parameters, *J. Geophys. Res.*, *100*(B10), 20,175–20,191, doi:10.1029/95JB02150.

Flowers, R. M., R. A. Ketcham, D. L. Shuster, and K. A. Farley (2009), Apatite (U–Th)/He thermochronometry using a radiation damage accumulation and annealing model, *Geochim. Cosmochim. Acta*, *73*(8), 2347–2365.

Fyhn, M. B. W., and P. V. Phach (2015), Late Neogene structural inversion around the northern Gulf of Tonkin, Vietnam: Effects from right-lateral displacement across the Red River fault zone, *Tectonics*, *34*, 290–312, doi:10.1002/2014TC003674.

Galbraith, R. F., and G. M. Laslett (1993), Statistical models for mixed fission track ages, *Nucl. Tracks Radiat. Meas.*, *21*(4), 459–470.

Galbraith, R. F., and P. F. Green (1990), Estimating the component ages in a finite mixture, *Int. J. Radiat. Appl. Instrum. Nucl. Tracks Radiat. Meas.*, *17*(3), 197–206.

Gallagher, K., R. Brown, and C. Johnson (1998), Fission track analysis and its applications to geological problems, *Ann. Rev. Earth Planet. Sci.*, *26*(1), 519.

Gan, W., P. Zhang, Z.-K. Shen, Z. Niu, M. Wang, Y. Wan, D. Zhou, and J. Cheng (2007), Present-day crustal motion within the Tibetan Plateau inferred from GPS measurements, *J. Geophys. Res.*, *112*, B08416, doi:10.1029/2005JB004120.

Gautheron, C., and L. Tassan-Got (2010), A Monte Carlo approach to diffusion applied to noble gas/helium thermochronology, *Chem. Geol.*, *273*(3–4), 212–224.

Gautheron, C., L. Tassan-Got, J. Barbarand, and M. Pagel (2009), Effect of alpha-damage annealing on apatite (U–Th)/He thermochronology, *Chem. Geol.*, *266*(3–4), 157–170.

Gleadow, A. J., and R. W. Brown (2000), Fission-track thermochronology and the long-term denudational response to tectonics, *Geomorphol. Global Tectonics*, 57–75.

Glotzbach, C., P. A. van der Beek, and C. Spiegel (2011), Episodic exhumation and relief growth in the Mont Blanc massif, Western Alps from numerical modelling of thermochronology data, *Earth Planet. Sci. Lett.*, *304*(3–4), 417–430.

Godard, V., R. Pik, J. Lave, R. Cattin, B. Tibari, J. de Sigoyer, M. Pubellier, and J. Zhu (2009), Late Cenozoic evolution of the central Longmen Shan, eastern Tibet: Insight from (U-Th)/He thermochronometry, *Tectonics*, *28*, TC5009, doi:10.1029/2008TC002407.

Hurford, A. J., and P. F. Green (1982), A users' guide to fission track dating calibration, *Earth Planet. Sci. Lett.*, *59*(2), 343–354.

Ketcham, R. A., C. Gautheron, and L. Tassan-Got (2011), Accounting for long alpha-particle stopping distances in (U–Th–Sm)/He geochronology: Refinement of the baseline case, *Geochim. Cosmochim. Acta*, *75*(24), 7779–7791.

Kirby, E., P. W. Reiners, M. A. Krol, K. X. Whipple, K. V. Hodges, K. A. Farley, W. Q. Tang, and Z. L. Chen (2002), Late Cenozoic evolution of the eastern margin of the Tibetan Plateau: Inferences from (40)Ar/(39)Ar and (U-Th)/He thermochronology, *Tectonics*, *21*(1), 1001, doi:10.1029/2000TC001246.

Lacassin, R., H. Maluski, P. H. Leloup, P. Tapponnier, C. Hinthong, K. Siribhakdi, S. Chuaviroj, and A. Charoenravat (1997), Tertiary diachronic extrusion and deformation of western Indochina: Structural and 40Ar/39Ar evidence from NW Thailand, *J. Geophys. Res.*, *102*(B5), 10,013–10,037, doi:10.1029/96JB03831.

Lai, Q. Z., L. Ding, H. W. Wang, Y. H. Yue, and F. L. Cai (2007), Constraining the stepwise migration of the eastern Tibetan Plateau margin by apatite fission track thermochronology, *Sci. China Ser. D Earth Sci.*, *50*(2), 172–183.

Lee, H.-Y., et al. (2003), Miocene Jiali faulting and its implications for Tibetan tectonic evolution, *Earth Planet. Sci. Lett.*, *205*(3–4), 185–194.

Leloup, P. H., T. M. Harrison, F. J. Ryerson, C. Wenji, L. Qi, P. Tapponnier, and R. Lacassin (1993), Structural, petrological and thermal evolution of a Tertiary ductile strike-slip shear zone, Diancang Shan, Yunnan, *J. Geophys. Res.*, *98*(B4), 6715–6743, doi:10.1029/92JB02791.

Leloup, P. H., R. Lacassin, P. Tapponnier, U. Schärer, D. Zhong, X. Liu, L. Zhang, S. Ji, and P. T. Trinh (1995), The Ailao Shan-Red River shear zone (Yunnan, China), Tertiary transform boundary of Indochina, *Tectonophysics*, *251*(1–4), 3–84.

Leloup, P. H., N. Arnaud, R. Lacassin, J. R. Kienast, T. M. Harrison, T. T. P. Trong, A. Replumaz, and P. Tapponnier (2001), New constraints on the structure, thermochronology, and timing of the Ailao Shan-Red River shear zone, SE Asia, *J. Geophys. Res.*, *106*(B4), 6683–6732, doi:10.1029/2000JB900322.

Li, H., and Y. Zhang (2013), Zircon U–Pb geochronology of the Konggar granitoid and migmatite: Constraints on the Oligo-Miocene tectono-thermal evolution of the Xianshuihe fault zone, East Tibet, *Tectonophysics*, *606*, 127–139.

Li, S., W. D. Mooney, and J. Fan (2006), Crustal structure of mainland China from deep seismic sounding data, *Tectonophysics*, *420*(1–2), 239–252.

Liang, S., W. Gan, C. Shen, G. Xiao, J. Liu, W. Chen, X. Ding, and D. Zhou (2013), Three-dimensional velocity field of present-day crustal motion of the Tibetan Plateau derived from GPS measurements, *J. Geophys. Res. Solid Earth*, *118*, 5722–5732, doi:10.1002/2013JB010503.

Lin, T.-H., C.-H. Lo, S.-L. Chung, F.-J. Hsu, M.-W. Yeh, T.-Y. Lee, J.-Q. Ji, Y.-Z. Wang, and D. Liu (2009), 40Ar/39Ar dating of the Jiali and Gaoligong shear zones: Implications for crustal deformation around the Eastern Himalayan Syntaxis, *J. Asian Earth Sci.*, *34*(5), 674–685.

Liu-Zeng, J., P. Tapponnier, Y. Gaudemer, and L. Ding (2008), Quantifying landscape differences across the Tibetan Plateau: Implications for topographic relief evolution, *J. Geophys. Res.*, *113*, F04018, doi:10.1029/2007JF000897.

Mancktelow, N. S., and B. Grasemann (1997), Time-dependent effects of heat advection and topography on cooling histories during erosion, *Tectonophysics*, *270*(3–4), 167–195.

Mériaux, A. S., J. Van der Woerd, P. Tapponnier, F. J. Ryerson, R. C. Finkel, C. Lasserre, and X. Xu (2012), The Pingding segment of the Altyn Tagh Fault (91°E): Holocene slip-rate determination from cosmogenic radionuclide dating of offset fluvial terraces, *J. Geophys. Res.*, *117*, B09406, doi:10.1029/2012JB009289.

Meyer, B., P. Tapponnier, L. Bourjot, F. Métivier, Y. Gaudemer, G. Peltzer, G. Shunmin, and C. Zhitai (1998), Crustal thickening in Gansu-Qinghai, lithospheric mantle subduction, and oblique, strike-slip controlled growth of the Tibet plateau, *Geophys. J. Int.*, *135*(1), 1–47.

Oskin, M. E. (2012), Tectonics: Reanimating eastern Tibet, *Nat. Geosci.*, *5*(9), 597–598.

Ouimet, W., K. Whipple, L. Royden, P. Reiners, K. Hodges, and M. Pringle (2010), Regional incision of the eastern margin of the Tibetan Plateau, *Lithosphere*, *2*(1), 50–63.

Paquette, J. L., and M. Tiepolo (2007), High resolution (5 μm) U–Th–Pb isotope dating of monazite with excimer laser ablation (ELA)-ICPMS, *Chem. Geol.*, *240*(3–4), 222–237.

Reid, A. J., A. P. Fowler, D. Phillips, and C. J. L. Wilson (2005a), Thermochronology of the Yidun Arc, central eastern Tibetan Plateau: Constraints from (40)Ar/(39)Ar K-feldspar and apatite fission track data, *J. Asian Earth Sci.*, *25*(6), 915–935.

Reid, A. J., C. J. L. Wilson, D. Phillips, and S. Liu (2005b), Mesozoic cooling across the Yidun Arc, central-eastern Tibetan Plateau: A reconnaissance Ar-40/Ar-39 study, *Tectonophysics*, *398*(1–2), 45–66.

Reiners, P. W., and M. T. Brandon (2006), Using thermochronology to understand orogenic erosion, *Annu. Rev. Earth Planet. Sci.*, *34*(1), 419–466.

Replumaz, A., and P. Tapponnier (2003), Reconstruction of the deformed collision zone Between India and Asia by backward motion of lithospheric blocks, *J. Geophys. Res.*, *108*(B6), 2285, doi:10.1029/2001JB000661.

Replumaz, A., R. Lacassin, P. Tapponnier, and P. Leloup (2001), Large river offsets and Plio-Quaternary dextral slip rate on the Red River fault (Yunnan, China), *J. Geophys. Res.*, *106*(B1), 819–836, doi:10.1029/2000JB900135.

Roger, F., S. Calassou, J. Lancelot, J. Malavieille, M. Mattauer, Z. Q. Xu, Z. W. Hao, and L. W. Hou (1995), Miocene emplacement and deformation of the Kongga-shan granite (Xianshui-he fault zone, West Sichuan, China)-geodynamic implications, *Earth Planet. Sci. Lett.*, *130*(1–4), 201–216.

Roger, F., M. Jolivet, and J. Malavieille (2008), Tectonic evolution of the Triassic fold belts of Tibet, *Compt. Rendus Geosci.*, *340*(2–3), 180–189.

Royden, L. H., B. C. Burchfiel, R. W. King, E. Wang, Z. L. Chen, F. Shen, and Y. P. Liu (1997), Surface deformation and lower crustal flow in eastern Tibet, *Science*, *276*(5313), 788–790.

Royden, L. H., B. C. Burchfiel, and R. D. van der Hilst (2008), The Geological evolution of the Tibetan Plateau, *Science*, *321*(5892), 1054–1058.

Sambridge, M. (1999a), Geophysical inversion with a neighbourhood algorithm-I. Searching a parameter space, *Geophys. J. Int.*, *138*(2), 479.

Sambridge, M. (1999b), Geophysical inversion with a neighbourhood algorithm--II. Appraising the ensemble, *Geophys. J. Int.*, *138*(3), 727.

Schoenbohm, L. M., K. X. Whipple, B. C. Burchfiel, and L. Chen (2004), Geomorphic constraints on surface uplift, exhumation, and plateau growth in the Red River region, Yunnan Province, China, *Geol. Soc. Am. Bull.*, *116*(7–8), 895–909.

Schoenbohm, L. M., B. C. Burchfiel, C. Liangzhong, and Y. Jiyun (2006), Miocene to present activity along the Red River fault, China, in the context of continental extrusion, upper-crustal rotation, and lower-crustal flow, *Geol. Soc. Am. Bull.*, *118*(5–6), 672–688.

Schwarz, G. (1978), Estimating the dimension of a model, *Ann. Stat.*, *6*(2), 461–464.

Stüwe, K., L. White, and R. Brown (1994), The influence of eroding topography on steady-state isotherms. Application to fission track analysis, *Earth Planet. Sci. Lett.*, *124*(1–4), 63–74.

Tapponnier, P., G. Peltzer, and R. Armijo (1986), *On the Mechanics of the Collision Between India and Asia*, *Geol. Soc. London Spec. Publ.*, *9*, pp. 113–157.

Tapponnier, P., Z. Q. Xu, F. Roger, B. Meyer, N. Arnaud, G. Wittlinger, and J. S. Yang (2001), Oblique stepwise rise and growth of the Tibet plateau, *Science*, *294*(5547), 1671–1677.

Tian, Y., B. P. Kohn, A. J. W. Gleadow, and S. Hu (2014), A thermochronological perspective on the morphotectonic evolution of the southeastern Tibetan Plateau, *J. Geophys. Res. Solid Earth*, *119*, 676–698, doi:10.1002/2013JB010429.

Valla, P. G., F. Herman, P. A. van der Beek, and J. Braun (2010), Inversion of thermochronological age-elevation profiles to extract independent estimates of denudation and relief history — I: Theory and conceptual model, *Earth Planet. Sci. Lett.*, *295*(3–4), 511–522.

Valli, F., et al. (2008), New U-Th/Pb constraints on timing of shearing and long-term slip-rate on the Karakorum fault, *Tectonics*, *27*, TC5007, doi:10.1029/2007TC002184.

Villaseñor, A., M. H. Ritzwoller, A. L. Levshin, M. P. Barmin, E. R. Engdahl, W. Spakman, and J. Trampert (2001), Shear velocity structure of central Eurasia from inversion of surface wave velocities, *Phys. Earth Planet. In.*, *123*(2–4), 169–184.

Wagner, G. A. (1981), Fission-track ages and their geological interpretation, *Nucl. Tracks*, *5*(1–2), 15–25.

Wang, C.-Y., H. Lou, P. G. Silver, L. Zhu, and L. Chang (2010), Crustal structure variation along 30°N in the eastern Tibetan Plateau and its tectonic implications, *Earth Planet. Sci. Lett.*, *289*(3–4), 367–376.

Wang, E., E. Kirby, K. P. Furlong, M. van Soest, G. Xu, X. Shi, P. J. J. Kamp, and K. V. Hodges (2012), Two-phase growth of high topography in eastern Tibet during the Cenozoic, *Nat. Geosci.*, *5*(9), 640–645.

Wang, S. F., X. M. Fang, D. W. Zheng, and E. C. Wang (2009), Initiation of slip along the Xianshuihe fault zone, eastern Tibet, constrained by K/Ar and fission-track ages, *Int. Geol. Rev.*, *51*(12), 1121–1131.

Wang, S., J. Guiguo, X. Tiande, T. Yuntao, Z. Dewen, and F. Xiaomin (2012), The Jinhe–Qinghe fault—An inactive branch of the Xianshuihe–Xiaojiang fault zone, Eastern Tibet, *Tectonophysics*, *544–545*, 93–102.

Wilson, C. J. L., and A. P. Fowler (2011), Denudational response to surface uplift in east Tibet: Evidence from apatite fission-track thermochronology, *Geol. Soc. Am. Bull.*, *123*(9–10), 1966–1987.

Wilson, C. J. L., M. J. Harrowfield, and A. J. Reid (2006), Brittle modification of Triassic architecture in eastern Tibet: Implications for the construction of the Cenozoic plateau, *J. Asian Earth Sci.*, *27*(3), 341–357.

Xu, G. Q., and P. J. J. Kamp (2000), Tectonics and denudation adjacent to the Xianshuihe Fault, eastern Tibetan Plateau: Constraints from fission track thermochronology, *J. Geophys. Res.*, *105*(B8), 19,231–19,251, doi:10.1029/2000JB900159.

Xu, X., X. Wen, G. Yu, R. Zheng, H. Luo, and B. Zheng (2005), Average slip rate, earthquake rupturing segmentation and recurrence behavior on the Litang fault zone, western Sichuan Province, China, *Sci. China Ser. D Earth Sci.*, *48*(8), 1183–1196.

Xu, X., X. Wen, G. Yu, G. Chen, Y. Klinger, J. Hubbard, and J. Shaw (2009), Coseismic reverse- and oblique-slip surface faulting generated by the 2008 Mw 7.9 Wenchuan earthquake, China, *Geology*, *37*(6), 515–518.

Zhang, P.-Z., Z. Shen, M. Wang, W. Gan, R. Bürgmann, P. Molnar, Q. Wang, Z. Niu, J. Sun, and J. Wu (2004), Continuous deformation of the Tibetan Plateau from global positioning system data, *Geology*, *32*(9), 809–812.

Zhou, S., L. Xu, J. Cui, X. Zhang, and J. Zhao (2005), Geomorphologic evolution and environmental changes in the Shaluli Mountain region during the Quaternary, *Chin. Sci. Bull.*, *50*(1), 52–57.